

SpaCRD: Multimodal Deep Fusion of Histology and Spatial Transcriptomics for Cancer Region Detection

Shuailin Xue^{1,2}, Jun Wan³, Lihua Zhang⁴, Wenwen Min^{1,2*}

¹School of Information Science and Engineering, Yunnan University, Kunming 650500, China

²Yunnan Key Laboratory of Intelligent Systems and Computing, Yunnan University, Kunming 650500, China

³School of Information Engineering, Zhongnan University of Economics and Law, Wuhan 430073, China

⁴School of Artificial Intelligence, School of Computer Science, Wuhan University, Wuhan 430072, China
xueshuailin@stu.ynu.edu.cn, junwan2014@whu.edu.cn, zhanglh@whu.edu.cn, minwenwen@ynu.edu.cn

Abstract

Accurate detection of cancer tissue regions (CTR) enables deeper analysis of the tumor microenvironment and offers crucial insights into treatment response. Traditional CTR detection methods, which typically rely on the rich cellular morphology in histology images, are susceptible to a high rate of false positives due to morphological similarities across different tissue regions. The groundbreaking advances in spatial transcriptomics (ST) provide detailed cellular phenotypes and spatial localization information, offering new opportunities for more accurate cancer region detection. However, current methods are unable to effectively integrate histology images with ST data, especially in the context of cross-sample and cross-platform/batch settings for accomplishing the CTR detection. To address this challenge, we propose SpaCRD, a transfer learning-based method that deeply integrates histology images and ST data to enable reliable CTR detection across diverse samples, platforms, and batches. Once trained on source data, SpaCRD can be readily generalized to accurately detect cancerous regions across samples from different platforms and batches. The core of SpaCRD is a category-regularized variational reconstruction-guided bidirectional cross-attention fusion network, which enables the model to adaptively capture latent co-expression patterns between histological features and gene expression from multiple perspectives. Extensive benchmark analysis on 23 matched histology-ST datasets spanning various disease types, platforms, and batches demonstrates that SpaCRD consistently outperforms existing eight state-of-the-art methods in CTR detection.

Code — <https://github.com/wenwenmin/SpaCRD>

1 Introduction

In clinical diagnosis and medical research, cancer tissue regions (CTR) detection is a critical step in developing treatment strategies for oncology patients (Lawrence et al. 2023). It not only aids in delineating surgical margins and precisely delivering radiation doses, but also provides essential spatial references for tumor microenvironment analysis (Khalighi et al. 2024; Xue, Wang et al. 2025). Prior research has commonly relied on manual annotations from pathologists

*Corresponding author.

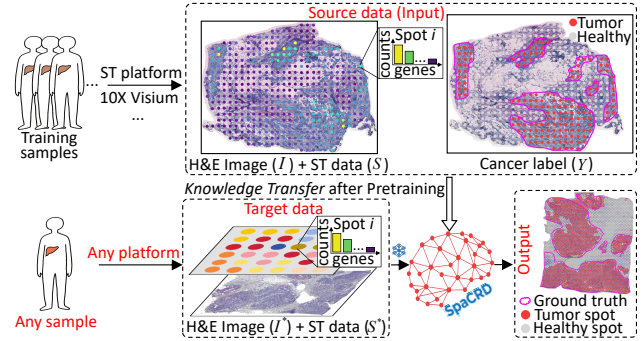


Figure 1: SpaCRD achieves accurate CTR detection across diverse samples and platforms&batches by deeply integrating histology images and ST data through transfer learning.

and traditional anomaly detection algorithms based on histology images analysis for CTR detection (Shmatko et al. 2022; Zingman, Stierstorfer et al. 2024). However, the former is limited by its high cost and time-consuming nature, while the latter suffers from poor accuracy due to the misleading morphological similarities across different tissue regions and inconsistent staining quality in histology images (Xue et al. 2025). As a result, neither is an ideal solution for CTR detection in clinical diagnosis and biomedical research.

As a revolutionary technology, spatial transcriptomics (ST) enables comprehensive profiling of transcripts across entire tissue sections while preserving their spatial locations, offering unprecedented capabilities for characterizing spatial heterogeneity and abnormal tissue architecture (Rao et al. 2021; Tian, Chen et al. 2023; Min et al. 2025). However, to precisely localize sequencing positions, ST requires additional processing steps during sequencing, which inevitably introduce background noise into the gene expression (Janssen et al. 2023). ST-based algorithms (Benjamin et al. 2024; Ferri-Borgogno et al. 2023; Shen et al. 2022) for various tasks are inevitably affected by the substantial noise inherent in ST data, which often prevents them from achieving optimal performance (Zahedi et al. 2024).

In addition, current tissue annotation methods (Zhang et al. 2024; Hu et al. 2023), which rely heavily on expert-defined prior knowledge, also detect CTR by aggregating the expression of marker genes. However, identifying re-

liable markers often requires extensive domain knowledge and experimental validation, and many cancer types lack well-defined markers that have been systematically identified, which further limits the generalizability and applicability of such approaches.

Effectively integrating histology and ST data to overcome morphological ambiguities and ST noise remains a major challenge in CTR detection (Maan et al. 2025). While some multimodal methods have been proposed, they suffer from critical shortcomings. For instance, SpaCell (Tan et al. 2020) fuses histology and ST data through simple feature concatenation, neglecting cross-modal interactions and global spatial context. STANDS (Xu et al. 2024) and MEATRD (Xu et al. 2025) follow the paradigm of traditional visual anomaly detection (Liu et al. 2023), but their reliance on reconstruction errors is ill-suited for structured cancer regions, which differ fundamentally from sparse anomalies in natural images (Seferbekova et al. 2023). Furthermore, these methods often fail to generalize across datasets due to batch heterogeneity, highlighting the need for more robust solutions.

Transfer learning offers a promising solution by leveraging knowledge learned from well-annotated source datasets to improve performance on heterogeneous target domains (Huang et al. 2025; Xue, Zhu et al. 2024). For example, several studies have used single-cell RNA-seq datasets from similar tissues as the source domain to guide cell type classification in ST datasets (target domain), effectively transferring cell-type signatures to spatial contexts (Yan et al. 2025; Hao et al. 2021). In CTR detection tasks, the target samples often originate from different platforms and experimental batches, resulting in substantial technical and biological variability. Motivated by the success of transfer learning, we apply transfer learning to align heterogeneous ST datasets and improve the generalizability of CTR detection across platforms and batches.

In this study, we propose **SpaCRD**, a multimodal deep fusion framework that integrates histology images and **S**patial transcriptomics data for **C**ancer **R**egion **D**etection. By leveraging transfer learning and a powerful multimodal deep fusion module, SpaCRD effectively mitigates technical and batch variations among affected individuals, achieving accurate and consistent CTR detection performance across different samples, platforms, and batches. Specifically, SpaCRD comprises a pretrained pathology foundation model, a modality-alignment representation learning, and a category-regularized **V**ariational **R**econstruction-guided **B**idirectional **C**ross-**A**ttention fusion network (VRBCA), which collectively enable end-to-end CTR detection from multimodal inputs. To the best of our knowledge, SpaCRD is the first framework that combines multimodal deep fusion with transfer learning for CTR detection. In summary, our contributions can be summarized as follows:

- We propose SpaCRD, a novel CTR detection framework leveraging multimodal deep fusion and transfer learning.
- SpaCRD mitigates technical and batch effects by aligning samples of the same disease type into a consistent representation space, thus enabling CTR detection across diverse samples and platforms&batches.

- We design a VRBCA network that reduces modality discrepancies, filters out noise, and stabilizes the fusion of ST data and histology images from complementary perspectives, while comprehensively modeling interactions among neighboring spots to facilitate the generation of compact and class-specific multimodal embeddings.
- Extensive benchmark on eleven breast cancer and twelve colorectal cancer datasets demonstrate that SpaCRD consistently outperforms eight state-of-the-art (SOTA) methods in CTR detection.

2 Methods ¹

As shown in Figure 2, our proposed SpaCRD framework consists of three main training stages: (1) **Modality-alignment representation learning**. We employ a pretrained pathology foundation model UNI (Chen et al. 2024) to extract informative histology image features. Meanwhile, we adopt a CLIP-based contrastive learning strategy (Radford et al. 2021) to align histology and ST modalities in a shared embedding space, effectively narrowing the modality gap and preparing for subsequent fusion. (2) **VRBCA Fusion Network**. VRBCA aims to learn compact and informative representations of the interactions between histology and ST modalities. (3) **Cancer likelihood estimation**. SpaCRD estimates a cancer likelihood score for each spot based on the compact representation yielded by VRBCA. The overall framework is summarized in the algorithm in Supplementary Material S2.

2.1 Modality-Alignment Representation Learning

First, we crop image patches from histology images based on spatial coordinates of each spot in ST data. Patch size is determined by spot diameter in ST data and the pixel resolution of the histology images (Jaume, Oldenburg et al. 2024). We adopt UNI, a pathology-specific foundation model pretrained on large-scale histology data, as our histological feature extractor. Due to its demonstrated ability to capture fine-grained histological structures, we skip the fine-tuning step to reduce computational overhead. Let $I = \{I_i \mid I_i \in \mathbb{R}^{l \times l \times 3}\}_{i=1}^n$ denote the set of image patches corresponding to all spots, where n is the total number of spots, and $l = d/r$, with d and r representing the spot diameter and the pixel resolution of the histology image, respectively. Then passing the entire set of patches I through the UNI model yields the H&E embeddings $X^{\text{img}} = \{\mathbf{x}_1^{\text{img}}, \dots, \mathbf{x}_n^{\text{img}}\}$ where

$$\mathbf{x}_i^{\text{img}} = f_{\text{UNI}}(I_i), \quad i = 1, \dots, n. \quad (1)$$

Let $X^{\text{gene}} = \{\mathbf{x}_1^{\text{gene}}, \dots, \mathbf{x}_n^{\text{gene}}\}$ represent the set of gene expression profiles in the ST data, where $\mathbf{x}_i^{\text{gene}}$ denotes the normalized expression vector of spot i . Given the substantial heterogeneity between image embeddings and gene expression data (Jaume, Vaidya et al. 2024), we employ a contrastive learning strategy to align the two modalities. By optimizing the contrastive loss, the model encourages paired

¹Related Work is in Supplementary Material S1 due to space limitation.

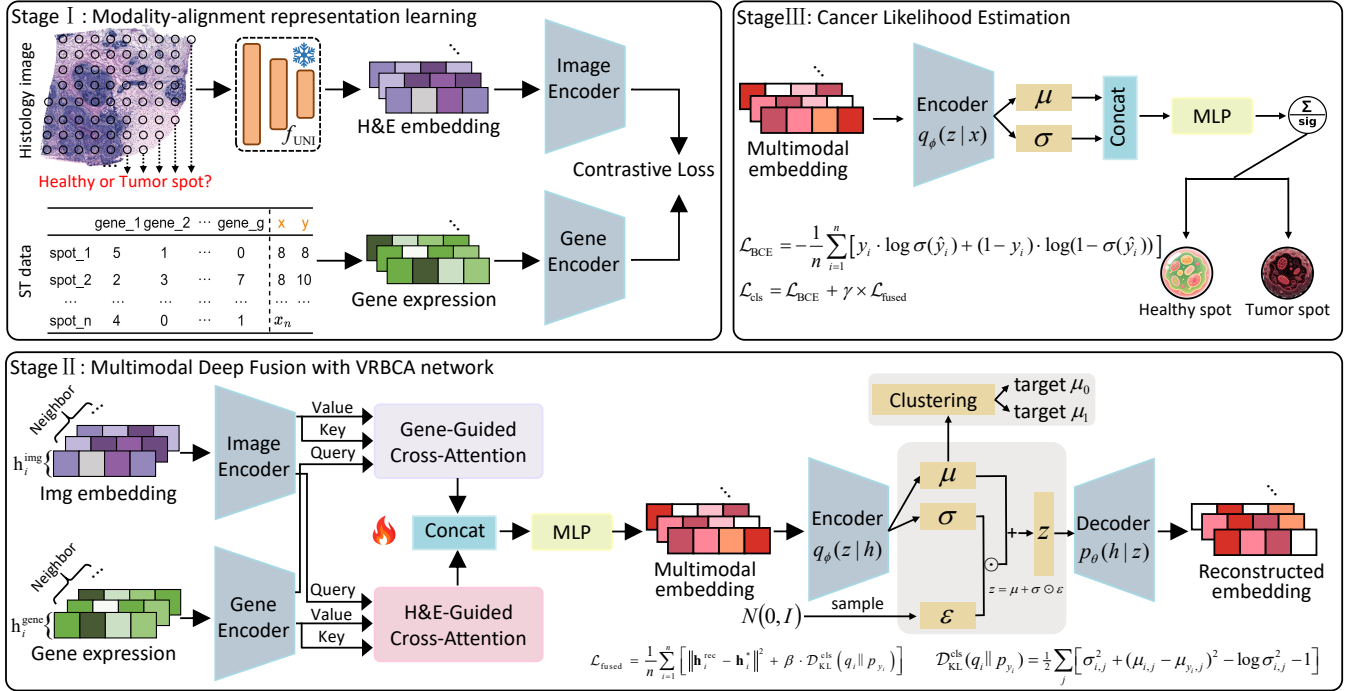


Figure 2: The framework of SpaCRD. Stage I: UNI is used to extract histology features, while modality-alignment representation learning aligns histology and ST modalities into a shared embedding space. Stage II: VRBCA integrates aligned histology and ST features into a compact and class-consistent embedding that captures biologically relevant cross-modal interactions. Stage III: The learned representation is used to estimate cancer likelihood scores for each spot.

image features and gene expression vectors from the same spatial location to be close in the latent space, while pushing apart those from different locations. This alignment reduces inconsistencies during the subsequent fusion process, ensuring a more stable and effective integration. We design two lightweight three-layer MLP-based encoders—an image encoder f_{c1} and a gene encoder f_{c2} —to perform the aforementioned alignment task:

$$\mathbf{h}_i^{\text{img}} = f_{c1}(\mathbf{x}_i^{\text{img}}), \quad \mathbf{h}_i^{\text{gene}} = f_{c2}(\mathbf{x}_i^{\text{gene}}). \quad (2)$$

To measure similarity between latent representations, we construct a similarity matrix using their scaled dot-product:

$$\mathbf{S}_{ij} = \frac{\mathbf{h}_i^{\text{img}} \cdot \mathbf{h}_j^{\text{gene}}}{\tau}, \quad \text{where } \|\mathbf{h}_i^{\text{img}}\| = \|\mathbf{h}_j^{\text{gene}}\| = 1, \quad (3)$$

with τ being a temperature parameter. Here, \mathbf{S}_{ii} denotes the similarity between the i -th image and its paired gene expression, while \mathbf{S}_{ij} for $i \neq j$ represents the similarity between unmatched pairs. Two directional InfoNCE loss components, $\mathcal{L}_{\text{img} \rightarrow \text{gene}}$ and $\mathcal{L}_{\text{gene} \rightarrow \text{img}}$, are independently computed using cross-entropy over similarity logits:

$$\mathcal{L}_{\text{img} \rightarrow \text{gene}} = -\frac{1}{n} \sum_{i=1}^n \log \frac{\exp(\mathbf{S}_{ii})}{\sum_{j=1}^n \exp(\mathbf{S}_{ij})}, \quad (4)$$

$$\mathcal{L}_{\text{gene} \rightarrow \text{img}} = -\frac{1}{n} \sum_{i=1}^n \log \frac{\exp(\mathbf{S}_{ii})}{\sum_{j=1}^n \exp(\mathbf{S}_{ji})}. \quad (5)$$

Finally, the total contrastive loss for this stage is defined as:

$$\mathcal{L}_{\text{contrast}} = \alpha \times \mathcal{L}_{\text{img} \rightarrow \text{gene}} + (1 - \alpha) \times \mathcal{L}_{\text{gene} \rightarrow \text{img}}, \quad (6)$$

where $\alpha \in [0, 1]$ controls the balance between the two directional losses. For all experiments, α is fixed at 0.5.

2.2 VRBCA Fusion Network

Following modality-alignment representation learning, the encoded features are fed into the VRBCA network. Overall, VRBCA utilizes a bidirectional cross-attention (BCA) mechanism to comprehensively model interactions between spots and to integrate the aligned features from multiple perspectives, followed by a category-regularized variational autoencoder (RVAE) for filtering out noise and promoting the generation of compact and class-specific embeddings. We define two independent Cross-Attention (CA) modules with identical architectures: gene-guided and H&E-guided CA blocks. Each module employs m parallel attention heads. For the i -th head, the query, key, and value matrices are derived through linear projections of the inputs:

$$Q_i = QW_i^Q, K_i = KW_i^K, V_i = VW_i^V. \quad (7)$$

Here, the shapes of W_i^Q , W_i^K , and W_i^V depend on the input modality and output embedding dimension d . The output of each head is computed as:

$$h_i = \text{Attention}(Q_i, K_i, V_i) = \text{softmax} \left(\frac{Q_i K_i^T}{\sqrt{d_h}} \right) V_i, \quad (8)$$

Metric	Method	Cross-samples											
		CRC_A1	CRC_A2	CRC_B1	CRC_B2	CRC_C1	CRC_C2	CRC_D1	CRC_D2	CRC_E1	CRC_E2	CRC_G1	CRC_G2
AUC	SimpleNet	0.491±0.163	0.518±0.098	0.488±0.036	0.481±0.055	0.440±0.047	0.488±0.070	0.518±0.050	0.435±0.036	0.429±0.129	0.580±0.103	0.506±0.082	0.463±0.047
	Spatial-ID	0.594±0.068	0.563±0.091	0.518±0.016	0.496±0.043	0.513±0.057	0.503±0.082	0.510±0.029	0.526±0.040	0.457±0.109	0.453±0.093	0.458±0.042	0.525±0.033
	STAGE	0.544±0.088	0.516±0.116	0.517±0.037	0.520±0.078	0.488±0.084	0.502±0.059	0.498±0.086	0.490±0.055	0.354±0.129	0.466±0.086	0.488±0.106	0.537±0.117
	STANDS	0.540±0.045	0.530±0.043	0.466±0.030	0.506±0.021	0.587±0.053	0.549±0.057	0.564±0.053	0.510±0.022	0.609±0.075	0.643±0.098	0.504±0.027	0.600±0.070
	TESLA	0.496±0.016	0.527±0.004	0.436±0.006	0.548±0.007	0.716±0.011	0.593±0.002	0.664±0.006	0.582±0.036	0.517±0.007	0.635±0.024	0.662±0.004	0.721±0.006
	iStar	0.444±0.025	0.436±0.027	0.517±0.002	0.514±0.005	0.733±0.004	0.638±0.004	0.654±0.008	0.672 ±0.061	0.505±0.014	0.593±0.051	0.781 ±0.002	0.799 ±0.005
	MEATRD	0.505±0.007	0.517±0.008	0.511±0.005	0.548±0.002	0.765 ±0.008	0.539±0.009	0.498±0.007	0.466±0.013	0.541±0.005	0.904±0.011	0.507±0.006	0.550±0.006
	SpaCell-Plus	0.821±0.012	0.762±0.010	0.678±0.006	0.713±0.004	0.761±0.014	0.713±0.012	0.625±0.034	0.472±0.018	0.799±0.024	0.816±0.015	0.638±0.028	0.733±0.016
	SpaCRD(ours)	0.953 ±0.002	0.925 ±0.004	0.824 ±0.005	0.897 ±0.003	0.895 ±0.007	0.880 ±0.010	0.789 ±0.020	0.603 ±0.022	0.966 ±0.006	0.961 ±0.007	0.853 ±0.005	0.888 ±0.003
	AP	SimpleNet	0.312±0.079	0.356±0.070	0.688±0.027	0.703±0.039	0.239±0.019	0.425±0.042	0.869±0.016	0.888±0.010	0.342±0.067	0.598±0.081	0.165±0.034
Spatial-ID		0.366±0.023	0.401±0.103	0.707±0.019	0.712±0.025	0.285±0.045	0.441±0.070	0.866±0.012	0.912±0.012	0.352±0.085	0.512±0.059	0.141±0.011	0.215±0.023
STAGE		0.300±0.054	0.335±0.092	0.686±0.025	0.712±0.044	0.257±0.047	0.419±0.043	0.852±0.031	0.913 ±0.010	0.295±0.052	0.504±0.064	0.164±0.045	0.240±0.089
STANDS		0.319±0.038	0.351±0.039	0.664±0.020	0.713±0.017	0.349±0.056	0.452±0.053	0.888±0.016	0.911±0.005	0.475±0.074	0.676±0.087	0.167±0.019	0.365±0.071
TESLA		0.317±0.008	0.421±0.024	0.574±0.004	0.613±0.005	0.376±0.004	0.536±0.006	0.874±0.003	0.813±0.017	0.427±0.004	0.642±0.022	0.425±0.002	0.300±0.004
iStar		0.252±0.007	0.290±0.008	0.695±0.002	0.717±0.003	0.410±0.002	0.503±0.003	0.900 ±0.002	0.911±0.010	0.372±0.006	0.597±0.033	0.349±0.007	0.433±0.007
MEATRD		0.272±0.005	0.329±0.005	0.693±0.003	0.742 ±0.005	0.518±0.023	0.439±0.007	0.816±0.005	0.902±0.002	0.403±0.005	0.892±0.015	0.194±0.003	0.236±0.004
SpaCell-Plus		0.714±0.035	0.695±0.016	0.731±0.008	0.738±0.018	0.577±0.020	0.670±0.005	0.773±0.026	0.836±0.022	0.748±0.009	0.797±0.023	0.620±0.036	0.624±0.011
SpaCRD(ours)		0.856 ±0.009	0.853 ±0.010	0.904 ±0.014	0.951 ±0.001	0.749 ±0.018	0.815 ±0.026	0.951 ±0.010	0.936 ±0.006	0.935 ±0.008	0.954 ±0.014	0.619 ±0.030	0.730 ±0.005
F1		SimpleNet	0.290±0.138	0.351±0.061	0.678±0.012	0.701±0.022	0.210±0.031	0.412±0.057	0.865±0.007	0.910±0.002	0.306±0.112	0.606±0.059	0.151±0.061
	Spatial-ID	0.359±0.044	0.364±0.086	0.688±0.005	0.705±0.026	0.283±0.066	0.418±0.064	0.864±0.006	0.918±0.002	0.326±0.123	0.510±0.078	0.116±0.019	0.217±0.049
	STAGE	0.294±0.093	0.327±0.109	0.721±0.016	0.726±0.031	0.226±0.084	0.417±0.045	0.816±0.011	0.911±0.002	0.242±0.107	0.520±0.054	0.150±0.080	0.234±0.116
	STANDS	0.300±0.048	0.344±0.041	0.671±0.011	0.711±0.010	0.326±0.064	0.465±0.043	0.866 ±0.003	0.915 ±0.002	0.466±0.071	0.638±0.081	0.160±0.031	0.298±0.079
	TESLA	0.412±0.010	0.345±0.015	0.427±0.022	0.106±0.021	0.513±0.007	0.612±0.004	0.853±0.002	0.809±0.029	0.546±0.030	0.594±0.033	0.384±0.006	0.528±0.018
	iStar	0.332±0.037	0.318±0.011	0.103±0.027	0.058±0.019	0.576±0.003	0.667±0.003	0.872±0.005	0.744±0.150	0.434±0.026	0.572±0.092	0.531±0.009	0.608 ±0.006
	MEATRD	0.270±0.011	0.320±0.010	0.690±0.004	0.723±0.002	0.526±0.017	0.452±0.014	0.866±0.002	0.911±0.001	0.406±0.012	0.851 ±0.016	0.156±0.011	0.239±0.013
	SpaCell-Plus	0.592±0.021	0.633 ±0.008	0.714±0.020	0.696±0.006	0.598±0.016	0.573±0.012	0.726±0.036	0.823±0.008	0.710±0.025	0.516 ±0.016	0.576±0.016	0.576±0.021
	SpaCRD(ours)	0.802 ±0.006	0.805 ±0.009	0.836 ±0.013	0.881 ±0.005	0.683 ±0.025	0.777 ±0.010	0.911 ±0.002	0.923 ±0.001	0.894 ±0.009	0.919 ±0.006	0.599 ±0.015	0.694 ±0.007

Table 1: Quantitative evaluation of SpaCRD for CTR detection on twelve colorectal cancer datasets compared to baselines. Each reported values are means ± standard deviations over five independent runs. Best results in bold, second-best underlined.

Metric	Method	Cross-samples								Cross-platforms&batches		
		STHBC_A	STHBC_B	STHBC_C	STHBC_D	STHBC_E	STHBC_F	STHBC_G	STHBC_H	ViHBC	XeHBC	IDC
AUC	SimpleNet	0.536±0.126	0.468±0.157	0.476±0.132	0.528±0.143	0.429±0.122	0.536±0.063	0.571±0.101	0.454±0.132	0.468±0.076	0.531±0.106	0.612±0.098
	Spatial-ID	0.544±0.045	0.534±0.135	0.471±0.083	0.451±0.085	0.477±0.102	0.496±0.107	0.558±0.094	0.438±0.117	0.436±0.067	0.593±0.081	0.502±0.080
	STAGE	0.536±0.126	0.468±0.157	0.476±0.132	0.528±0.143	0.429±0.122	0.536±0.063	0.571±0.101	0.474±0.190	0.444±0.067	0.575±0.054	0.605±0.068
	STANDS	0.535±0.053	0.449±0.058	0.510±0.008	0.507±0.038	0.524±0.027	0.575±0.036	0.564±0.046	0.451±0.072	0.629±0.102	0.532±0.037	0.566±0.092
	TESLA	0.724±0.008	0.586±0.018	0.551±0.012	0.605±0.011	0.627±0.002	0.705±0.022	0.697±0.014	0.729±0.009	0.692±0.025	0.748±0.026	0.476±0.021
	iStar	0.788±0.013	0.674±0.020	0.591±0.017	0.668±0.016	0.741 ±0.004	0.672±0.024	0.714±0.017	0.681±0.011	0.736±0.032	0.842 ±0.038	0.531±0.009
	MEATRD	0.604±0.007	0.963±0.003	0.783±0.010	0.837±0.006	0.442±0.013	0.468±0.023	0.774±0.029	0.614±0.024	0.517±0.002	0.472±0.004	0.496±0.002
	SpaCell-Plus	0.929±0.010	0.950±0.012	0.773±0.019	0.844±0.009	0.668±0.056	0.774±0.056	0.826±0.021	0.812±0.017	0.784±0.028	0.818±0.034	0.803±0.009
	SpaCRD(ours)	0.979 ±0.002	0.993 ±0.002	0.795 ±0.025	0.952 ±0.003	0.909 ±0.011	0.913 ±0.008	0.923 ±0.004	0.969 ±0.004	0.900 ±0.029	0.931 ±0.008	0.891 ±0.006
	AP	SimpleNet	0.907±0.038	0.226±0.062	0.724±0.070	0.511±0.097	0.536±0.083	0.870±0.024	0.412±0.082	0.287±0.062	0.603±0.047	0.570±0.054
Spatial-ID		0.909±0.017	0.264±0.122	0.729±0.038	0.453±0.047	0.565±0.076	0.855±0.042	0.383±0.075	0.285±0.036	0.571±0.051	0.405±0.035	0.582±0.044
STAGE		0.907±0.038	0.226±0.062	0.724±0.070	0.511±0.097	0.536±0.083	0.870±0.024	0.412±0.082	0.309±0.155	0.559±0.039	0.529±0.047	0.643±0.053
STANDS		0.889±0.019	0.179±0.018	0.731±0.023	0.451±0.037	0.557±0.024	0.859±0.017	0.345±0.029	0.290±0.016	0.692±0.094	0.575±0.060	0.573±0.070
TESLA		0.842±0.004	0.354±0.012	0.803±0.004	0.657±0.006	0.683±0.008	0.829±0.006	0.576±0.016	0.568±0.004	0.754±0.028	0.620±0.012	0.697±0.007
iStar		0.956±0.003	0.332±0.020	0.783±0.009	0.632±0.011	0.761±0.004	0.903±0.007	0.543±0.029	0.460±0.005	0.788±0.021	0.723±0.014	0.621±0.007
MEATRD		0.916±0.017	0.948±0.007	0.916±0.005	0.832±0.013	0.554±0.010	0.848±0.008	0.653±0.024	0.459±0.011	0.631±0.005	0.317±0.008	0.595±0.003
SpaCell-Plus		0.991±0.002	0.853±0.036	0.904±0.007	0.845±0.011	0.757±0.043	0.949±0.017	0.745±0.049	0.745±0.013	0.846±0.015	0.726±0.018	0.847±0.006
SpaCRD(ours)		0.998 ±0.000	0.980 ±0.003	0.923 ±0.011	0.961 ±0.001	0.911 ±0.013	0.983 ±0.003	0.867 ±0.007	0.947 ±0.005	0.930 ±0.037	0.859 ±0.021	0.914 ±0.006
F1		SimpleNet	0.903±0.006	0.197±0.127	0.738±0.046	0.499±0.103	0.535±0.067	0.863±0.008	0.385±0.099	0.260±0.081	0.604±0.044	0.592±0.087
	Spatial-ID	0.905±0.009	0.225±0.164	0.740±0.029	0.437±0.068	0.569±0.063	0.859±0.013	0.385±0.080	0.227±0.069	0.590±0.030	0.430±0.030	0.611±0.055
	STAGE	0.903±0.006	0.197±0.127	0.738±0.046	0.499±0.103	0.535±0.067	0.863±0.008	0.385±0.099	0.330±0.172	0.597±0.039	0.437±0.034	0.674±0.037
	STANDS	0.898±0.005	0.111±0.043	0.718±0.019	0.453±0.031	0.566±0.015	0.863±0.003	0.341±0.050	0.079±0.035	0.699±0.059	0.604±0.046	0.582±0.049
	TESLA	0.820±0.015	0.476±0.020	0.404±0.005	0.579±0.022	0.643±0.004	0.663±0.018	0.676±0.016	0.498±0.008	0.641±0.034	0.586±0.016	0.510±0.026
	iStar	0.803±0.028	0.483±0.026	0.389±0.026	0.536±0.044	0.701±0.006	0.700±0.027	0.618±0.023	0.582±0.009	0.668±0.065	0.689±0.020	0.135±0.033
	MEATRD	0.907±0.022	0.886±0.021	0.843 ±0.007	0.752 ±0.008	0.536±0.013	0.850±0.005	0.648±0.017	0.453±0.027	0.630±0.001	0.333±0.007	0.597±0.003
	SpaCell-Plus	0.956±0.003	0.778±0.044	0.827±0.016	0.730±0.013	0.672±0.042	0.902 ±0.010	0.668±0.043	0.645±0.022	0.766±0.025	0.667±0.036	0.758±0.009
	SpaCRD(ours)	0.975 ±0.002	0.926 ±0.012	0.818±0.004	0.878 ±0.009	0.866 ±0.011	0.929 ±0.005	0.789 ±0.007	0.860 ±0.009	0.867 ±0.014	0.795 ±	

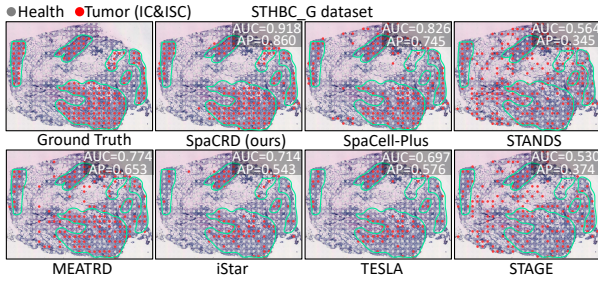


Figure 3: ATR detection results of SpaCRD and other baselines on the STHBC_G dataset. Green outlines indicate pathologist-annotated CTR. Gray and red dots represent normal and cancerous spots, respectively.

regularized variational reconstruction objective, which imposes semantic structure on the latent space and facilitates the learning of class-discriminative multimodal features. Specifically, we extend the VAE framework by introducing learnable class-specific latent centers, forming a structure-aware latent prior. VRBCA encodes the fused multimodal representation into latent variables via an encoder f_{enc} , producing mean μ_i and log-variance $\log \sigma_i^2$. A latent vector $z_i \sim \mathcal{N}(\mu_i, \sigma_i^2)$ is sampled and decoded by f_{dec} to reconstruct the multimodal representation, yielding \hat{h}_i^* :

$$\mu_i, \log \sigma_i^2 = f_{\text{enc}}(\mathbf{h}_i^*), \quad (13)$$

$$z_i = \mu_i + \sigma \odot \epsilon, \epsilon \sim \mathcal{N}(\mathbf{0}, \mathbf{I}), \quad (14)$$

$$\hat{h}_i^* = f_{\text{dec}}(z_i). \quad (15)$$

The training objective for the fused representation is defined as:

$$\mathcal{L}_{\text{fused}} = \frac{1}{n} \sum_{i=1}^n \left[\left\| \hat{h}_i^* - \mathbf{h}_i^* \right\|^2 + \beta \cdot \mathcal{D}_{\text{KL}}^{\text{cls}}(q_i \| p_{y_i}) \right], \quad (16)$$

$$\mathcal{D}_{\text{KL}}^{\text{cls}}(q_i \| p_{y_i}) = \frac{1}{2} \sum_j \left[\sigma_{i,j}^2 + (\mu_{i,j} - \mu_{y_i,j})^2 - \log \sigma_{i,j}^2 - 1 \right], \quad (17)$$

where $q_i = \mathcal{N}(\mu_i, \text{diag}(\sigma_i^2))$ is the approximate posterior, $p_{y_i} = \mathcal{N}(\mu_{y_i}, \mathbf{I})$ is the class-specific Gaussian prior with learnable mean μ_{y_i} based on the label $y_i \in \{0, 1\}$. In all experiments, we set $\beta = 0.5$.

2.3 Cancer Likelihood Discriminator

After the modality-aware fusion by the VRBCA network, the cancer likelihood discriminator estimates the probability of each spot being cancerous. Specifically, the mean μ_i and log-variance $\log \sigma_i^2$ produced by the trained encoder f_{enc} of VRBCA, are concatenated and fed into a two-layer MLP classifier to predict cancer likelihood. The loss function for the discriminator combines BCE loss with the fused loss:

$$\mathcal{L}_{\text{BCE}} = -\frac{1}{n} \sum_{i=1}^n [y_i \cdot \log \sigma(\hat{y}_i) + (1 - y_i) \cdot \log(1 - \sigma(\hat{y}_i))], \quad (18)$$

$$\mathcal{L}_{\text{cls}} = \mathcal{L}_{\text{BCE}} + \gamma \times \mathcal{L}_{\text{fused}}, \quad (19)$$

where \hat{y}_i denotes the predicted score by the classifier indicating how likely the spot is cancerous. The hyperparameters γ is fixed to 0.1 in the experiments. At inference time, benefiting from the regularized latent representations, our model

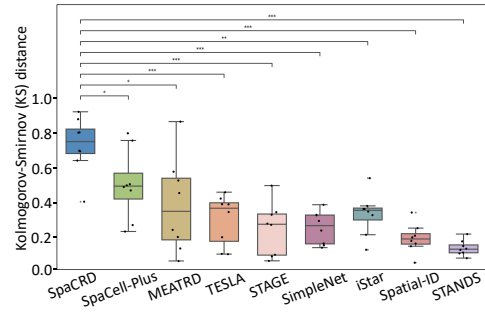


Figure 4: Comparison of the KS distances between predicted cancer likelihood distributions in healthy and tumor regions.

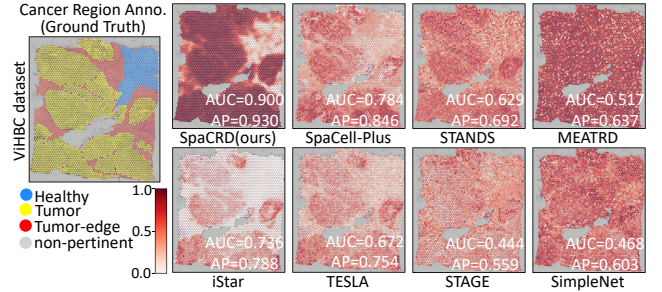


Figure 5: Visualization of cancer likelihood scores predicted by SpaCRD and other baselines on the ViHBC dataset.

effectively separates cancerous and normal spots in the predicted score space. To automatically determine a classification threshold, we fit a two-component Gaussian Mixture Model (GMM) to the distribution of predicted scores and use the intersection point between the two Gaussian components as the decision threshold, as detailed in Supplementary Material S3.

3 Experiments

3.1 Experimental Setup

Datasets. We evaluate SpaCRD on five datasets comprising a total of 23 matched histology-ST datasets (termed tissue sections). Among them, two multi-section datasets—STHBC (Andersson, Larsson et al. 2021) and CRC (Valdeolivas, Amberg et al. 2024)—are used for cross-sample evaluation, while the remaining three—10XHBC, XcHBC (Janesick, Shelansky et al. 2023), and IDC—are used for cross-platforms&batches evaluation (see Supplementary Material S4 for detailed dataset description and preprocessing of the 23 tissue sections).

Implementation Details. We conducted all experiments using a single NVIDIA RTX 3090 GPU (24GB), with the development environment based on PyTorch 2.1.1 and Python 3.11.5. Detailed network architectures, training schedules, and implementation settings are provided in Supplementary Material S5.

Baselines and Evaluation Metrics. To evaluate the performance of SpaCRD, we compared it with eight SOTA

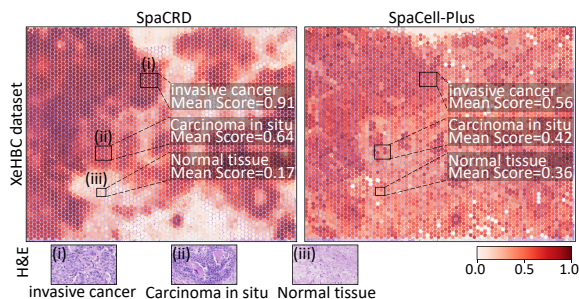


Figure 6: Cancer likelihood scores predicted by SpaCRD and the best-performing baseline method, SpaCell-Plus on the XeHBC dataset.

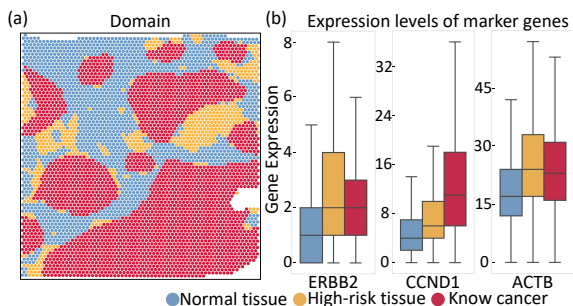


Figure 7: In the IDC dataset, SpaCRD-predicted high-score spots labeled non-cancerous exhibit elevated breast cancer marker expression, suggesting potential early lesions.

methods, including five multimodal-based: MEATRD (Xu et al. 2025), STANDS (Xu et al. 2024), SpaCell (Tan et al. 2020), iStar (Zhang et al. 2024), TESLA (Hu et al. 2023); two ST-based: STAGE (Li et al. 2024), Spatial-ID (Shen et al. 2022); and one image-based: SimpleNet (Liu et al. 2023). For evaluation metrics, AUC, AP, F1-score, and KS distance are used to assess the performance of all methods. Supplementary Materials S6 and S7 provide the detailed descriptions for baselines and evaluation metrics.

3.2 Cross-Samples Cancer Region Detection

To evaluate the cross-samples CTR detection capability of SpaCRD, we conducted leave-one-out cross-validation on the twelve colorectal cancer (CRC_[A1-G2]) and eight human breast cancer (STHBC_[A-H]) datasets. As shown in Table 1 and 2 (Cross-samples), SpaCRD achieves the best performance in AUC, AP, and F1-score, surpassing all baselines. Across 20 datasets covering both breast cancer and colorectal cancer, SpaCRD consistently outperforms the second-best method, achieving an average improvement of 13.5%, 14.1%, and 14.0% in AUC, AP, and F1-score, respectively. Methods that rely on prior knowledge, such as iStar and TESLA, perform suboptimally, possibly due to limitations in generalizing predefined features across datasets. Similarly, methods like MEATRD and STANDS, which adopt training strategies inspired by conventional anomaly detection in computer vision, struggle to capture the continuous and structured nature of cancer regions. SpaCell-

Plus lacks effective integration of histology and ST data, resulting in inferior performance compared with our method. We further demonstrate the superiority of SpaCRD over the baselines by visualizing the CTR detection results on the STHBC datasets (Figure 3 and Supplementary Material S8.1). Finally, we evaluated the distributional divergence between predicted cancer likelihood scores in healthy and tumor regions across the eight STHBC datasets using the Kolmogorov–Smirnov (KS) distance. As shown in Figure 4, SpaCRD exhibited the strongest separation between healthy and tumor regions across most STHBC datasets (Median: SpaCRD=0.754, SpaCell-Plus=0.494, MEATRD=0.348).

3.3 Cross-Platforms&batches Cancer Region Detection

We further evaluated the performance of SpaCRD on the challenging task of cross-platforms&batches CTR detection. We trained SpaCRD on the STHBC dataset generated from the ST platform and tested it on datasets from other platforms, including ViHBC (Visium), IDC (Visium) and XeHBC (Xenium) datasets. As shown in Table 2 (Cross-platforms&batches), SpaCRD achieves superior performance over all baselines across all test datasets, with average improvements of 12.1%, 11.8%, and 13.8% in AUC, AP, and F1-score, respectively, compared to the second-best method. In addition, we comparative analyzed the predicted cancer likelihood scores of SpaCRD and other baseline methods on the ViHBC dataset. As shown in Figure 5, SpaCRD accurately distinguishes cancer regions from healthy tissues. Moreover, compared to baselines, it effectively separates the tumor-edge in certain regions, with predicted scores falling between those of the cancer and healthy spots. SpaCell-Plus and STANDS also identified ATR regions; however, the separation between cancer and healthy regions was less distinct compared to SpaCRD. iStar and TESLA were able to predict parts of the cancer regions; however, their predictions were incomplete and failed to capture the full extent of the lesions. Distribution analysis using histograms and violin plots further confirms SpaCRD’s ability to distinguish between biologically distinct tissue regions (see Supplementary Material S8.2). Consistent with the findings on the ViHBC dataset, visualization analysis of the XeHBC and IDC datasets shows that the cancer likelihood scores predicted by SpaCRD are highly consistent with ground truth (Supplementary Material S8.1). These results suggest SpaCRD mitigates technical and batch effects by integrating image and ST data into a unified latent space, enabling robust, generalizable CTR detection across diverse platforms and batches.

3.4 Downstream Analysis: Detection of Potential Lesion Regions

We systematically evaluated SpaCRD’s ability to stratify cancer severity by analyzing its predicted likelihood scores. On the XeHBC dataset generated from Xenium platform, SpaCRD achieved average scores of 0.91 (invasive cancer), 0.64 (carcinoma in situ), and 0.17 (normal tissue), effectively distinguishing malignancy levels (Figure 6). Heatmap

Extractor	Cross-samples						Cross-platforms&batches								
	STHBC			CRC			10XHBC			IDC			XeHBC		
	AUC	AP	F1	AUC	AP	F1	AUC	AP	F1	AUC	AP	F1	AUC	AP	F1
w/ Swin-Tiny	0.880	0.923	0.838	0.820	0.795	0.793	0.689	0.751	0.728	0.501	0.601	0.601	0.718	0.465	0.501
w/ ResNet50	0.878	0.908	0.836	0.830	0.800	0.794	0.637	0.697	0.701	0.596	0.649	0.657	0.656	0.698	0.691
w/ HIPT	0.885	0.912	0.827	0.822	0.796	0.793	0.784	0.829	0.786	0.399	0.525	0.546	0.771	0.736	0.742
w/ UNI (ours)	0.929	0.946	0.880	0.869	0.854	0.810	0.900	0.930	0.867	0.891	0.914	0.854	0.931	0.859	0.795

Table 3: Ablation study of histology feature extractors conducted across all datasets used in this study.

Model	HBC(eleven datasets)			CRC(twelve datasets)		
	AUC	AP	F1	AUC	AP	F1
Image-based	0.789	0.752	0.733	0.606	0.557	0.553
ST-based	0.832	0.815	0.747	0.782	0.793	0.755
w/o BCA	0.849	0.833	0.788	0.797	0.774	0.759
w/o RVAE	0.887	0.898	0.817	0.831	0.816	0.795
w/o VRBCA	0.815	0.796	0.734	0.771	0.746	0.717
w/o CL	0.892	0.886	0.828	0.824	0.807	0.776
Ours	0.923	0.934	0.869	0.869	0.854	0.810

Table 4: Ablation study of modalities and fusion modules conducted across all datasets used in this study.

Metric	Parameter α			Parameter β		
	0.0	0.5	1.0	0.1	0.5	1.0
AUC	0.908	0.923	0.916	0.863	0.923	0.920
AP	0.912	0.934	0.929	0.895	0.934	0.931
F1	0.843	0.869	0.863	0.828	0.869	0.867
Metric	Parameter γ			neighboring spots		
	0.0	0.1	1.0	4	6	10
AUC	0.772	0.923	0.919	0.908	0.923	0.912
AP	0.768	0.934	0.931	0.896	0.934	0.925
F1	0.794	0.869	0.856	0.844	0.869	0.858

Table 5: Sensitivity analysis of key hyperparameter across eleven breast cancer datasets. Gray : default settings.

visualization confirmed clear stratification, with invasive regions showing the highest intensity, followed by carcinoma in situ and normal tissue. In contrast, SpaCell-Plus produced less discriminative scores (0.56, 0.42, and 0.36, respectively), failing to separate carcinoma in situ from normal tissue. Other baselines also exhibited dispersed, inconsistent score distributions (Supplementary Material S8.1). Notably, these distinctions are often imperceptible in histology images, suggesting SpaCRD’s scores may reflect tumor aggressiveness. Finally, we examined the spots in the IDC dataset that received high predicted scores from SpaCRD but were annotated as non-cancerous in the manual labels (Figure 7(a), orange spots). Remarkably, these spots exhibit significantly elevated expression of canonical breast cancer marker genes (e.g., ERBB2 (Harari et al. 2000), CCND1 (Valla et al. 2022), and ACTB (Majidzadeh-A et al. 2011), Figure 7(b)), compared to normal tissue. This suggests that SpaCRD captures spatial regions warranting clinical investigation and potentially of pathological relevance.

3.5 Ablation Studies

To assess the contributions of key components in SpaCRD, we conducted ablation studies on all datasets, focusing on the Histology feature extractor, unimodal inputs, and module ablations. All reported results are averaged over five independent runs. **Since some experiments involve aggregat-**

ing scores across multiple datasets, we report the overall mean values without standard deviations for consistency.

Impact of Extractors. We replaced UNI with ResNet50 (He et al. 2016) and Swin-Tiny (Liu, Lin et al. 2021) pre-trained on natural images, and HIPT (Chen, Chen et al. 2022) pretrained on pathological images. As shown in Table 3, UNI yields the best performance. Notably, the performance of other extractors drops markedly in the cross-platforms&batches evaluation, likely due to large variations in histology images that hinder their ability to capture core fine-grained features.

Impact of Modalities and Fusion Modules. We assessed the contributions of different input modalities and the fusion module by (i) using only histology or ST data, and (ii) removing key fusion components, including the multimodal deep fusion module (BCA), the regularized reconstruction-guided denoising module (RVAE), and the modality-alignment representation learning (CL). As shown in Table 4, removing any modality input or module results in suboptimal performance.

3.6 Robustness and Efficiency Analysis

- **Sensitivity Analysis:** We conducted sensitivity analyses on eleven breast cancer datasets, covering key hyperparameter α , β , and γ , as well as the number of neighboring spots selected in the BCA model (Table 5). Detailed analyses are provided in Supplementary Material S8.3.
- **Empirical Efficiency Analysis:** We analyzed the cost of SpaCRD and baselines by evaluating the number of parameters, runtime, and memory usage. The detailed results in Supplementary Material S8.4 indicate that SpaCRD maintains an acceptable computational cost.
- **Small-Sample Training Analysis:** Additional experiments show that even when training set contains less than 10% of the spots in test set, SpaCRD maintains stable performance in cross-platform CTR detection, demonstrating strong generalization and data efficiency (see Supplementary Material S8.5 for detailed results).

4 Conclusion

In this study, we present SpaCRD, a multimodal deep fusion and transfer learning-based framework that integrates histology images and ST data for accurate and generalizable CTR detection across samples and platforms&batches. SpaCRD leverages the proposed VRBCA fusion module, synergistically optimized through contrastive learning objectives, to dynamically integrate histology images and gene expression

features in both image-to-gene and gene-to-image directions. By jointly attending to both gene-to-image and image-to-gene signals and modeling interactions among neighboring spots, VRBCA ensures comprehensive feature integration, while its variational reconstruction mechanism filters out noise and promotes compact and class-consistent embeddings. Extensive evaluations across diverse datasets from multiple platforms demonstrate the strong generalization capability of SpaCRD. In addition, SpaCRD may serve as a promising tool for medical researchers by enabling the stratification of cancer severity and revealing spatial regions that may warrant further clinical investigation. Supplementary Materials can be found at the code link.

Acknowledgments

The work was supported in part by the Program of Yunnan Key Laboratory of Intelligent Systems and Computing (No. 202405AV340009) and the National Natural Science Foundation of China (Nos. 62262069, 62571555).

References

- 10x Genomics. 2020. Breast Cancer: Ductal Carcinoma In Situ, Lobular carcinoma In Situ, Invasive Carcinoma (Block A Section 1). <https://www.10xgenomics.com/datasets/human-breast-cancer-block-a-section-1-1-standard-1-1-0>.
- Andersson, A.; Larsson, L.; et al. 2021. Spatial deconvolution of HER2-positive breast cancer delineates tumor-associated cell type interactions. *Nature communications*, 12(1): 6012.
- Benjamin, K.; Bhandari, A.; Kepple, J. D.; Qi, R.; Shang, Z.; Xing, Y.; An, Y.; Zhang, N.; Hou, Y.; Crockford, T. L.; et al. 2024. Multiscale topology classifies cells in subcellular spatial transcriptomics. *Nature*, 630(8018): 943–949.
- Chen, R. J.; Chen, C.; et al. 2022. Scaling vision transformers to gigapixel images via hierarchical self-supervised learning. In *Proceedings of the IEEE/CVF conference on computer vision and pattern recognition*, 16144–16155.
- Chen, R. J.; Ding, T.; Lu, M. Y.; Williamson, D. F.; Jaume, G.; Song, A. H.; Chen, B.; Zhang, A.; Shao, D.; Shaban, M.; et al. 2024. Towards a general-purpose foundation model for computational pathology. *Nature Medicine*, 30(3): 850–862.
- Ferri-Borgogno, S.; Zhu, Y.; Sheng, J.; Burks, J. K.; Gomez, J. A.; Wong, K. K.; Wong, S. T.; and Mok, S. C. 2023. Spatial transcriptomics depict ligand–receptor cross-talk heterogeneity at the tumor-stroma interface in long-term ovarian cancer survivors. *Cancer research*, 83(9): 1503–1516.
- Hao, Y.; Hao, S.; Andersen-Nissen, E.; Mauck, W. M.; Zheng, S.; Butler, A.; Lee, M. J.; Wilk, A. J.; Darby, C.; Zager, M.; et al. 2021. Integrated analysis of multimodal single-cell data. *Cell*, 184(13): 3573–3587.
- Harari, et al. 2000. Molecular mechanisms underlying ErbB2/HER2 action in breast cancer. *Oncogene*, 19(53): 6102–6114.
- He, K.; Zhang, X.; Ren, S.; and Sun, J. 2016. Deep residual learning for image recognition. In *Proceedings of the IEEE conference on computer vision and pattern recognition*, 770–778.
- Hu, J.; Coleman, K.; Zhang, D.; Lee, E. B.; Kadara, H.; Wang, L.; and Li, M. 2023. Deciphering tumor ecosystems at super resolution from spatial transcriptomics with TESLA. *Cell Systems*, 14(5): 404–417.
- Hu, J.; Li, X.; et al. 2021. SpaGCN: Integrating gene expression, spatial location and histology to identify spatial domains and spatially variable genes by graph convolutional network. *Nature methods*, 18(11): 1342–1351.
- Hu, Y.; Xie, M.; Li, Y.; Rao, M.; Shen, W.; Luo, C.; Qin, H.; Baek, J.; and Zhou, X. M. 2024. Benchmarking clustering, alignment, and integration methods for spatial transcriptomics. *Genome Biology*, 25(1): 212.
- Huang, T.; Liu, T.; Babadi, M.; Jin, W.; and Ying, R. 2025. Scalable generation of spatial transcriptomics from histology images via whole-slide flow matching. In *International Conference on Machine Learning*, 1–16. PmlR.
- Janesick, A.; Shelansky, R.; et al. 2023. High resolution mapping of the tumor microenvironment using integrated single-cell, spatial and in situ analysis. *Nature communications*, 14(1): 8353.
- Janssen, P.; Kliesmete, Z.; Vieth, B.; Adiconis, X.; Simmons, S.; Marshall, J.; McCabe, C.; Heyn, H.; Levin, J. Z.; Enard, W.; et al. 2023. The effect of background noise and its removal on the analysis of single-cell expression data. *Genome biology*, 24(1): 140.
- Jaume, G.; Oldenburg, L.; et al. 2024. Transcriptomics-guided slide representation learning in computational pathology. In *Proceedings of the IEEE/CVF Conference on Computer Vision and Pattern Recognition*, 9632–9644.
- Jaume, G.; Vaidya, A.; et al. 2024. Modeling dense multimodal interactions between biological pathways and histology for survival prediction. In *Proceedings of the IEEE/CVF Conference on Computer Vision and Pattern Recognition*, 11579–11590.
- Khalighi, S.; Reddy, K.; Midya, A.; Pandav, K. B.; Madabhushi, A.; and Abedalthagafi, M. 2024. Artificial intelligence in neuro-oncology: advances and challenges in brain tumor diagnosis, prognosis, and precision treatment. *NPJ precision oncology*, 8(1): 80.
- Kingma, D. P.; Welling, M.; et al. 2014. Auto-encoding variational bayes. In *International Conference on Learning Representations*, 1–14.
- Kipf, T. N.; and Welling, M. 2017. Semi-supervised classification with graph convolutional networks. In *International Conference on Learning Representations*, 1–14.
- Lawrence, R.; Watters, M.; Davies, C. R.; Pantel, K.; and Lu, Y.-J. 2023. Circulating tumour cells for early detection of clinically relevant cancer. *Nature Reviews Clinical Oncology*, 20(7): 487–500.
- Li, S.; Gai, K.; Dong, K.; Zhang, Y.; and Zhang, S. 2024. High-density generation of spatial transcriptomics with STAGE. *Nucleic Acids Research*, 52(9): 4843–4856.
- Liu, Z.; Lin, Y.; et al. 2021. Swin transformer: Hierarchical vision transformer using shifted windows. In *Proceedings of the IEEE/CVF international conference on computer vision*, 10012–10022.

- Liu, Z.; Zhou, Y.; Xu, Y.; and Wang, Z. 2023. Simplenet: A simple network for image anomaly detection and localization. In *Proceedings of the IEEE/CVF conference on computer vision and pattern recognition*, 20402–20411.
- Maan, H.; Ji, Z.; Sicheri, E.; Tan, T. J.; Selega, A.; Gonzalez, R.; Krishnan, R.; WANG, B.; and Campbell, K. R. 2025. Multi-modal disentanglement of spatial transcriptomics and histopathology imaging. In *Learning Meaningful Representations of Life (LMRL) Workshop at ICLR 2025*, 1–35. PmLR.
- Majidzadeh-A; et al. 2011. TFRC and ACTB as the best reference genes to quantify Urokinase Plasminogen Activator in breast cancer. *BMC research notes*, 4(1): 215.
- Min, W.; Shi, Z.; Zhang, J.; Wan, J.; and Wang, C. 2024. Multimodal contrastive learning for spatial gene expression prediction using histology images. *Briefings in Bioinformatics*, 25(6): bbae551.
- Min, W.; et al. 2025. SpaViT: self-supervised prediction of high-resolution spatial transcriptomics with vision transformer. *Tsinghua Science and Technology*.
- Radford, A.; Kim, J. W.; Hallacy, C.; Ramesh, A.; Goh, G.; Agarwal, S.; Sastry, G.; Askell, A.; Mishkin, P.; Clark, J.; et al. 2021. Learning transferable visual models from natural language supervision. In *International conference on machine learning*, 8748–8763. PmLR.
- Rao, A.; Barkley, D.; França, G. S.; and Yanai, I. 2021. Exploring tissue architecture using spatial transcriptomics. *Nature*, 596(7871): 211–220.
- Seferbekova, Z.; Lomakin, A.; Yates, L. R.; and Gerstung, M. 2023. Spatial biology of cancer evolution. *Nature Reviews Genetics*, 24(5): 295–313.
- Shen, R.; Liu, L.; Wu, Z.; Zhang, Y.; Yuan, Z.; Guo, J.; Yang, F.; Zhang, C.; Chen, B.; Feng, W.; et al. 2022. Spatial-ID: a cell typing method for spatially resolved transcriptomics via transfer learning and spatial embedding. *Nature communications*, 13(1): 7640.
- Shmatko, A.; Ghaffari Laleh, N.; Gerstung, M.; and Kather, J. N. 2022. Artificial intelligence in histopathology: enhancing cancer research and clinical oncology. *Nature cancer*, 3(9): 1026–1038.
- Sohn, K.; Li, C.-L.; Yoon, J.; Jin, M.; and Pfister, T. 2021. Learning and evaluating representations for deep one-class classification. In *International Conference on Learning Representations*, 1–14.
- Tan, X.; Su, A.; Tran, M.; and Nguyen, Q. 2020. SpaCell: integrating tissue morphology and spatial gene expression to predict disease cells. *Bioinformatics*, 36(7): 2293–2294.
- Tian, L.; Chen, F.; et al. 2023. The expanding vistas of spatial transcriptomics. *Nature Biotechnology*, 41(6): 773–782.
- Valdeolivas, A.; Amberg, B.; et al. 2024. Profiling the heterogeneity of colorectal cancer consensus molecular subtypes using spatial transcriptomics. *NPJ precision oncology*, 8(1): 10.
- Valla, M.; Klæstad, E.; Ytterhus, B.; and Bofin, A. M. 2022. CCND1 amplification in breast cancer-associations with proliferation, histopathological grade, molecular subtype and prognosis. *Journal of mammary gland biology and neoplasia*, 27(1): 67–77.
- Vaswani, A.; Shazeer, N.; Parmar, N.; Uszkoreit; et al. 2017. Attention is all you need. In *Advances in neural information processing systems*, volume 30, 1–11.
- Velickovic, P.; Cucurull, G.; Casanova; et al. 2018. Graph attention networks. In *International Conference on Learning Representations*, 1–12.
- Xu, K.; Lu, Y.; Hou, S.; Liu, K.; Du, Y.; Huang, M.; Feng, H.; Wu, H.; and Sun, X. 2024. Detecting anomalous anatomic regions in spatial transcriptomics with STANDS. *Nature Communications*, 15(1): 8223.
- Xu, K.; Wu, Q.; Lu, Y.; Zheng, Y.; Li, W.; Tang, X.; Wang, J.; and Sun, X. 2025. MeatrD: Multimodal anomalous tissue region detection enhanced with spatial transcriptomics. In *Proceedings of the AAAI Conference on Artificial Intelligence*, volume 39, 12918–12926.
- Xue, S.; Wang, C.; et al. 2025. Inferring Super-Resolved Gene Expression by Integrating Histology Images and Spatial Transcriptomics with HISTEX. In *International Conference on Medical Image Computing and Computer-Assisted Intervention*, 296–306. Springer.
- Xue, S.; Zhu, F.; Chen, J.; and Min, W. 2025. Inferring single-cell resolution spatial gene expression via fusing spot-based spatial transcriptomics, location, and histology using GCN. *Briefings in Bioinformatics*, 26(1): bbae630.
- Xue, S.; Zhu, F.; et al. 2024. stEnTrans: transformer-based deep learning for spatial transcriptomics enhancement. In *International Symposium on Bioinformatics Research and Applications*, 63–75. Springer.
- Yan, C.; Zhang, Y.; Feng, J.; et al. 2025. Triple-effect correction for Cell Painting data with contrastive and domain-adversarial learning. *Nature Communications*, 16(1): 6886.
- Zahedi, R.; Ghamsari, R.; Argha, A.; Macphillamy, C.; Beheshti, A.; Alizadehsani, R.; Lovell, N. H.; Lotfollahi, M.; and Alinejad-Rokny, H. 2024. Deep learning in spatially resolved transcriptomics: a comprehensive technical view. *Briefings in Bioinformatics*, 25(2): bbae082.
- Zhang, D.; Schroeder, A.; Yan, H.; Yang, H.; Hu, J.; Lee, M. Y.; Cho, K. S.; Susztak, K.; Xu, G. X.; Feldman, M. D.; et al. 2024. Inferring super-resolution tissue architecture by integrating spatial transcriptomics with histology. *Nature Biotechnology*, 42(9): 1372–1377.
- Zhao, E.; Stone, M. R.; et al. 2021. Spatial transcriptomics at subspot resolution with BayesSpace. *Nature biotechnology*, 39(11): 1375–1384.
- Zingman, I.; Stierstorfer, B.; et al. 2024. Learning image representations for anomaly detection: application to discovery of histological alterations in drug development. *Medical Image Analysis*, 92: 103067.

Supplementary Material

S1 Related Works

S1.1 Cancer Tissue Region Detection

Early CTR detection relied on traditional anomaly detection in histology images. For example, SimpleNet (Liu et al. 2023) generates pseudo-anomalies by perturbing visual embeddings with noise and employs a hyperplane-based discriminator for anomaly separation. However, such methods heavily rely on effective representation learning (Sohn et al. 2021), struggling to handle batch effects commonly present in pathological images.

Spatial-ID (Shen et al. 2022) is the first method to perform CTR detection using spatial transcriptomics (ST) data alone, which integrates transfer learning with a deep neural network trained on scRNA-seq data and employs a graph convolutional network (Kipf and Welling 2017) to incorporate spatial context for improved cell typing and anomaly identification. However, due to its exclusive reliance on ST data, Spatial-ID is vulnerable to noise and dropout, which may lead to the misclassification of normal regions as abnormal when subtle expression similarities exist among healthy.

Super-resolution annotation methods that rely on expert-defined priors, such as iStar (Zhang et al. 2024), leverage pretrained HIPT (Chen, Chen et al. 2022) models to extract hierarchical histological features, followed by a feed-forward neural network to model histology and gene expression jointly, and then use an expert-defined list of marker genes to infer CTR. TESLA (Hu et al. 2023) adopts a similar CTR detection strategy to iStar, but generates super-resolved gene expression by leveraging a Euclidean metric that integrates spatial proximity and histological similarity. The heavy dependence on expert-defined priors significantly constrains the wide applicability of these approaches.

SpaCell (Tan et al. 2020) designs two independent autoencoders (Kingma, Welling et al. 2014) to integrate histology images and ST data into a unified latent representation for CTR detection. However, it lacks deep multimodal interaction and fails to generalize to cross-platform and cross-batch CTR detection scenarios. STANDS (Xu et al. 2024) encodes histology and gene expression data using a hybrid network of graph attention (GAT) (Velickovic et al. 2018) and ResNet-GAT, followed by a Transformer-based fusion module to identify CTR. Following the training strategy of STANDS, MEATRD (Xu et al. 2025) combines MobileUNet, graph neural networks, and Transformer modules (Vaswani et al. 2017) in a unified architecture, and follows the conventional visual anomaly detection strategy by detecting CTR through reconstruction errors. However, due to the continuous and structured nature of cancer regions, reconstruction-error-based STANDS and MEATRD often fail to effectively distinguish them from normal tissue.

S1.2 Multimodal Integration of Histology and Spatial Transcriptomics

Beyond CTR detection, multimodal integration of histology images and ST data has also been developed for related tasks, such as gene expression prediction (Min et al.

2024), and spatial domain identification (Hu et al. 2024; Hu, Li et al. 2021).

mclSTExp (Min et al. 2024) predicts spatial gene expression from H&E-stained whole-slide images by aligning histology and transcriptomics via contrastive learning. However, it performs only modality alignment without learning joint representations, effectively mapping one modality to the other rather than achieving true fusion.

SpaGCN (Hu, Li et al. 2021) integrates gene expression and histology via a 3D weighted graph and applies Louvain clustering on GCN features to identify spatial domains. However, as these methods typically prioritize maximizing spatial variability, they are not well suited for CTR detection, which demands higher accuracy and interpretability.

In summary, existing multimodal approaches focus primarily on tasks like gene expression prediction or spatial domain identification, often employing alignment or simple aggregation techniques. While pioneering, these methods do not explicitly address the high-stakes demands of high-accuracy CTR detection, which requires robust fusion and precise, interpretable identification of clinically relevant boundaries, moving beyond maximizing general spatial variance.

S2 Algorithm Framework of SpaCRD

The overall training and inference pipeline of SpaCRD is summarized in Algorithm 1.

S3 Determining Cancer Likelihood Score Threshold

To convert the predicted continuous scores (ranging from 0 to 1) into binary labels indicating cancerous versus healthy regions, we adopt a thresholding approach based on a Gaussian Mixture Model (GMM). This method is particularly suitable when the prediction score distribution is bimodal and manual thresholding proves unreliable.

We assume that the distribution of the model output scores \hat{y} can be approximated by a mixture of two univariate Gaussian distributions, corresponding to the underlying healthy and cancerous tissue classes, respectively. The probability density function is given by:

$$p(\hat{y}) = \pi_1 \cdot \mathcal{N}(\hat{y} | \mu_1, \sigma_1^2) + \pi_2 \cdot \mathcal{N}(\hat{y} | \mu_2, \sigma_2^2), \quad (\text{S1})$$

where $\mathcal{N}(\hat{y} | \mu, \sigma^2)$ denotes the Gaussian (normal) probability density function:

$$\mathcal{N}(\hat{y} | \mu, \sigma^2) = \frac{1}{\sqrt{2\pi\sigma^2}} \exp\left(-\frac{(\hat{y} - \mu)^2}{2\sigma^2}\right). \quad (\text{S2})$$

In the mixture model, $\pi_1, \pi_2 \in (0, 1)$ are the mixing coefficients (with $\pi_1 + \pi_2 = 1$), and (μ_k, σ_k^2) are the mean and variance of the k -th component ($k = 1, 2$).

The parameters $\Theta = \{\pi_k, \mu_k, \sigma_k^2\}_{k=1}^2$ are estimated from the data using the Expectation-Maximization (EM) algorithm, which maximizes the log-likelihood of the observed scores $\{\hat{y}_i\}_{i=1}^n$:

Algorithm 1 SpaCRD: Spatial Cancer Region Detection Framework

Input: Histology patches $I = \{I_i \mid I_i \in \mathbb{R}^{l \times l \times 3}\}_{i=1}^n$; gene expression $X^{\text{gene}} = \{X_1^{\text{gene}}, \dots, X_n^{\text{gene}}\}$, spot coordinates $S = \{s_i\}_{i=1}^n$

Definition: Pre-trained pathology-specific foundation model f_{UNI} ; Image encoder f_{c1} ; Gene encoder f_{c2} ; Two directional InfoNCE loss $\mathcal{L}_{\text{img} \rightarrow \text{gene}}$ and $\mathcal{L}_{\text{gene} \rightarrow \text{img}}$; Gene-guided cross-attention network CA_{gene} ; H&E-guided cross-attention network CA_{img} ; Feedforward fusion network f ; RVAE encoder f_{enc} and decoder f_{dec} ; L2 loss function \mathcal{L}_2 ; category-regularized KL divergence loss function $\mathcal{D}_{\text{KL}}^{\text{cls}}$; Cross-entropy loss function \mathcal{L}_{BCE} ; MLP-based classifier f_{cls} .

Output: Cancer likelihood scores $\hat{y} = \{\hat{y}_i\}_{i=1}^n$, binary labels $\hat{c} = \{\hat{c}_i\}_{i=1}^n$

```

1: for each batch  $b$  do
2:    $X_b^{\text{img}} = \{f_{\text{UNI}}(I_i) \mid i \in \mathcal{B}_b\}$ 
3: end for
4: for each batch  $b$  do
5:    $H_b^{\text{img}} \leftarrow f_{c1}(X_b^{\text{img}}), H_b^{\text{gene}} \leftarrow f_{c2}(X_b^{\text{gene}})$ 
6:    $\mathcal{L}_{\text{contrast}} = \alpha \times \mathcal{L}_{\text{img} \rightarrow \text{gene}} + (1 - \alpha) \times \mathcal{L}_{\text{gene} \rightarrow \text{img}}$ 
7:   Update parameters of  $f_{c1}, f_{c2}$  using  $\mathcal{L}_{\text{contrast}}$ 
8: end for
9: for each batch  $b$  do
10:   $H_{bi}^{\text{img}} \leftarrow$  image features of spot  $i$  and  $s$  neighbors
11:   $H_{bi}^{\text{gene}} \leftarrow$  gene features of spot  $i$  and  $s$  neighbors
12:   $H_b^m = \{H_{bi}^m \mid i \in \mathcal{B}_b, H_{bi}^m \in \mathbb{R}^{(s+1) \times d}\}, m \in \{\text{img}, \text{gene}\}$ 
13:   $Z_b^{\text{img}} = \text{CA}_{\text{img}}(H_b^{\text{img}}, H_b^{\text{gene}}, H_b^{\text{gene}})$ 
14:   $Z_b^{\text{gene}} = \text{CA}_{\text{gene}}(H_b^{\text{gene}}, H_b^{\text{img}}, H_b^{\text{img}})$ 
15:   $H_b^* = f(Z_b^{\text{img}}[:, 0, :], Z_b^{\text{gene}}[:, 0, :])$ 
16:   $(\mu_b, \log \sigma_b^2) \leftarrow f_{\text{enc}}(H_b^*)$ 
17:  Sample latent  $Z_b \sim \mathcal{N}(\mu_b, \sigma_b^2), \hat{H}_b^* \leftarrow f_{\text{dec}}(Z_b)$ 
18:   $\mathcal{L}_{\text{fused}} = \mathcal{L}_2(H_b^*, \hat{H}_b^*) + \beta \cdot \mathcal{D}_{\text{KL}}^{\text{cls}}(q_b \| p_y)$ 
19:  Update parameters of  $\text{CA}_{\text{img}}, \text{CA}_{\text{gene}}, f, f_{\text{enc}}, f_{\text{dec}}$  using  $\mathcal{L}_{\text{fused}}$ 
20: end for
21: for each batch  $b$  do
22:   $\hat{y}_b = \{f_{\text{cls}}(\mu_i \parallel \log \sigma_i^2) \mid i \in \mathcal{B}_b\}$ 
23:   $\mathcal{L}_{\text{cls}} = \mathcal{L}_{\text{BCE}} + \gamma \cdot \mathcal{L}_{\text{fused}}$ 
24:  Update parameters of  $\text{CA}_{\text{img}}, \text{CA}_{\text{gene}}, f, f_{\text{enc}}, f_{\text{dec}}, f_{\text{cls}}$  using  $\mathcal{L}_{\text{cls}}$ 
25: end for
26: Fit GMM to  $\hat{y}$  and compute threshold  $\tau$ 
27: for  $i = 1$  to  $n$  do
28:   $\hat{c}_i \leftarrow \mathbb{I}(\hat{y}_i \geq \tau)$ 
29: end for
30: return  $\hat{y}, \hat{c}$ 

```

$$\log p(\hat{y} \mid \Theta) = \sum_{i=1}^n \log \left[\pi_1 \cdot \mathcal{N}(\hat{y}_i \mid \mu_1, \sigma_1^2) + \pi_2 \cdot \mathcal{N}(\hat{y}_i \mid \mu_2, \sigma_2^2) \right]. \quad (\text{S3})$$

By expanding both sides of the equality and simplifying, we obtain the nonlinear equation to solve for the decision threshold τ , which corresponds to the intersection point(s) of the two Gaussian components:

$$\pi_1 \cdot \mathcal{N}(\hat{y} \mid \mu_1, \sigma_1^2) = \pi_2 \cdot \mathcal{N}(\hat{y} \mid \mu_2, \sigma_2^2). \quad (\text{S4})$$

Expanding the Gaussian densities explicitly, this can be written as:

$$\frac{\pi_1}{\sqrt{2\pi\sigma_1^2}} \exp\left(-\frac{(\hat{y} - \mu_1)^2}{2\sigma_1^2}\right) = \frac{\pi_2}{\sqrt{2\pi\sigma_2^2}} \exp\left(-\frac{(\hat{y} - \mu_2)^2}{2\sigma_2^2}\right). \quad (\text{S5})$$

Taking the natural logarithm of both sides yields:

$$\log\left(\frac{\pi_1}{\sigma_1}\right) - \frac{(\hat{y} - \mu_1)^2}{2\sigma_1^2} = \log\left(\frac{\pi_2}{\sigma_2}\right) - \frac{(\hat{y} - \mu_2)^2}{2\sigma_2^2}. \quad (\text{S6})$$

Rearranging terms gives a quadratic equation in \hat{y} :

$$a\hat{y}^2 + b\hat{y} + c = 0, \quad (\text{S7})$$

where the coefficients (a, b, c) are determined analytically from $(\pi_k, \mu_k, \sigma_k^2)$:

$$\begin{aligned} a &= \frac{1}{2\sigma_2^2} - \frac{1}{2\sigma_1^2}, \\ b &= \frac{\mu_2}{\sigma_2^2} - \frac{\mu_1}{\sigma_1^2}, \\ c &= \frac{\mu_1^2}{2\sigma_1^2} - \frac{\mu_2^2}{2\sigma_2^2} + \ln\left(\frac{\sigma_2\pi_1}{\sigma_1\pi_2}\right). \end{aligned} \quad (\text{S8})$$

This quadratic equation may have two real roots. Among these, we select the solution that lies within the interval $(\min(\mu_1, \mu_2), \max(\mu_1, \mu_2))$ as the threshold τ :

$$\tau \in (\min(\mu_1, \mu_2), \max(\mu_1, \mu_2)).$$

In rare cases where the two components have significant overlap or the EM fitting is degenerate, this solver may fail to yield a real root within the interval. This fallback ensures the method remains robust even when the ideal solution is not identifiable. In such cases, we define the threshold heuristically as the midpoint between the two means:

$$\tau = \frac{\mu_1 + \mu_2}{2}. \quad (\text{S9})$$

Once the threshold τ is determined, binary labels are assigned to each spot based on whether the predicted score exceeds the threshold:

$$\hat{c}_i = \begin{cases} 1, & \text{if } \hat{y}_i \geq \tau \quad (\text{cancer}) \\ 0, & \text{otherwise} \quad (\text{healthy}) \end{cases}. \quad (\text{S10})$$

The proposed GMM-based thresholding is fully data-driven and adaptive to the distribution of each sample's scores, providing a robust and interpretable approach, especially beneficial in weakly-supervised settings and datasets with heterogeneous annotation quality.

S4 Datasets

S4.1 Dataset Descriptions

As shown in Table S1, we conducted extensive benchmark experiments on datasets from two types of cancer to demonstrate the accuracy and generalizability of SpaCRD:

Human Breast Cancer: The human breast cancer (HBC) datasets used in this study consist of eight HBC datasets generated from the older ST platform (denoted as STHBC_A to STHBC_H) (Andersson, Larsson et al. 2021), one HBC dataset generated from the 10X Visium platform (denoted as ViHBC) (10x Genomics 2020), one human invasive ductal carcinoma (IDC) dataset generated from the 10X Visium platform (denoted as IDC) (Zhao, Stone et al. 2021), and one HBC dataset generated from the Xenium platform (denoted as XeHBC) (Janesick, Shelansky et al. 2023). The eight STHBC_[A-H] datasets were derived from different oncology patients. For cross-samples CTR detection, we performed leave-one-out cross-validation on the eight STHBC_[A-H] datasets. For cross-platforms&batches CTR detection, the model was trained on the STHBC datasets and tested on the ViHBC, XeHBC, and IDC datasets.

Human Colorectal Cancer: To further demonstrate the generalizability of SpaCRD in CTR detection, we additionally conducted experiments on twelve colorectal cancer datasets generated from the 10X Visium platform (denoted as CRC_[A1-E2, G1, G2]) (Valdeolivas, Amberg et al. 2024). The twelve CRC datasets represent samples from multiple tumor patients, where pairs like A1 and A2 correspond to one patient, B1 and B2 to another, and so on. For cross-sample CTR detection, we performed a patient-wise leave-one-out cross-validation on the twelve CRC datasets.

Histology Image: Each ST dataset is accompanied by a corresponding histology image, spatial coordinates of all spots relative to the image, the spot radius, and the pixel resolution of the histology image.

S4.2 Dataset Preprocessing

All datasets were preprocessed through a standardized pipeline. Spots located outside tissue regions were removed based on the “in_tissue” flag provided in the spatial transcriptomics metadata. Gene expression matrices were normalized to a total count of 10,000 per spot and log-transformed using the SCANPY package. Finally, the top 3,000 highly variable genes (HVGs) were selected using the Seurat v3 method implemented in SCANPY.

Since the XeHBC dataset is at single-cell resolution and thus differs from the spot-based ST data distribution, we performed an aggregation preprocessing step to make it comparable. Specifically, we aggregated cells based on the Visium spot size, diameter, and center-to-center distance by grouping all cells covered within each spot area:

$$s_i = \sum_{k \in \Gamma_i} c_k, \quad (\text{S11})$$

where s_i represents the gene expression of spot S_i , and Γ_i represents the set of all cells covered by spot S_i . This process generated data comparable to the 10X Visium spatial resolution.

S5 Implementation Details

We conducted all experiments using a single NVIDIA RTX 3090 GPU (24GB), with the development environment based on PyTorch 2.1.1 and Python 3.11.5. The three training stages were run for 100, 50, and 50 epochs, respectively, using the Adam optimizer with a uniform learning rate of 0.00001 across all stages. For contrastive learning, both the image and gene encoder comprise two hidden layers with 1024 and 512 units, followed by a projection layer that maps the features into a shared 512-dimensional latent space. Batch normalization, ReLU activation, and dropout with a rate of 0.2 are applied to each hidden layer. The BCA module consists of two asymmetric cross-attention layers followed by a linear fusion layer. Each cross-attention layer employs 8 attention heads with an embedding dimension of 512. The multimodal features from both directions are concatenated and projected through a linear fusion layer into a unified 512-dimensional representation, followed by Layer-Norm. For RVAE module, the encoder consists of two fully connected layers with 256 and 128 units, each followed by a ReLU activation, and then two parallel linear layers that output the latent mean μ and log-variance $\log \sigma^2$, both of dimension 64. The decoder is symmetric to the encoder, comprising fully connected layers that reverse this transformation to reconstruct the input. Two learnable cluster centers are initialized from Gaussian distributions with means -0.5 and $+0.5$, respectively. Finally, the latent mean μ and log-variance $\log \sigma^2$ are concatenated and fed into a two-layer MLP-based classifier with a hidden size of 64 to predict cancer likelihood scores. For the bidirectional cross-attention mechanism, we select the top 6 nearest neighboring spots for each spot based on Euclidean distance to enable deep contextual information fusion.

S6 Baseline methods

MEATRD identifies disease regions by learning to reconstruct multimodal features from normal tissues and detecting regions with high reconstruction errors. It first extracts visual features from 32×32 histology patches using Mobile-UNet and encodes the corresponding gene expression profiles with a two-layer MLP. These dual-modal representations are then fused within 3-hop neighborhood subgraphs using a Masked Graph Dual-Attention Transformer. The resulting 128-dimensional feature is compressed into a 64-dimensional bottleneck, from which the histology image and gene expression are independently reconstructed using a ResNet and a GNN, respectively. MEATRD is trained on normal tissue samples, and disease regions are identified during inference based on reconstruction errors. In our implementation, to evaluate MEATRD on the STHBC_[A-H], ViHBC, XeHBC, and IDC datasets for CTR detection, the model was trained on eight human healthy breast datasets, denoted as HHB_[v03-v10]. For colorectal cancer datasets (CRC_[A1-E2, G1, G2]), MEATRD was trained on two normal human colon (CRC_F1 and CRC_F2) datasets, and inference was performed separately on each CRC_[A1-E2, G1, G2] dataset. All other settings and hyperparameters followed the original MEATRD implementation as described

Datasets	Tissue	Spots	Cancer Ratio	Platform
STHBC_A	Breast cancer (Invasive cancer & Cancer in situ)	346	89.9%	ST
STHBC_B	Breast cancer (Invasive cancer)	295	22.0%	
STHBC_C	Breast cancer (Invasive cancer)	176	73.9%	
STHBC_D	Breast cancer (Invasive cancer)	306	48.1%	
STHBC_E	Breast cancer (Invasive cancer)	587	57.9%	
STHBC_F	Breast cancer (Invasive cancer)	691	85.7%	
STHBC_G	Breast cancer (Invasive cancer & Cancer in situ)	467	34.3%	
STHBC_H	Breast cancer (Invasive cancer & Cancer in situ)	613	33.1%	
XeHBC	Breast cancer (Ductal carcinoma in situ & invasive carcinoma)	4,050	34.9%	Xenium
ViHBC	Breast cancer (Lobular carcinoma in situ & Invasive Carcinoma)	3,798	61.9%	Visium
IDC	Breast cancer (invasive carcinoma & carcinoma in situ)	4,727	59.9%	
CRC_A1	Colorectal cancer	2,203	27.0%	
CRC_A2	Colorectal cancer	2,385	31.2%	
CRC_B1	Colorectal cancer	2,317	67.0%	
CRC_B2	Colorectal cancer	1,803	70.9%	
CRC_C1	Colorectal cancer	328	25.6%	
CRC_C2	Colorectal cancer	1,048	42.3%	
CRC_D1	Colorectal cancer	691	86.1%	
CRC_D2	Colorectal cancer	1,219	91.2%	
CRC_E1	Colorectal cancer	1,192	36.9%	
CRC_E2	Colorectal cancer	387	54.0%	
CRC_G1	Colorectal cancer	2,128	15.9%	
CRC_G2	Colorectal cancer	1,691	20.5%	

Table S1: Summary of all experimental datasets used in this study.

in the original paper.

STANDS formulates disease region detection as an anomaly detection task based on generative adversarial reconstruction. A GAN generator is trained on a normal reference dataset to reconstruct both gene expression and histology features. For each spot, a multimodal representation is constructed by fusing a gene embedding (obtained via GAT) and a histology embedding (extracted using ResNet-GAT) through a Transformer module, resulting in a 512-dimensional latent feature. The decoder then reconstructs both the original gene expression profile and the corresponding 112×112 histology patch. After training, the reconstruction error—measured as the cosine distance between the original and reconstructed features—is computed on the target dataset and used as the disease likelihood score. To evaluate STANDS in our experiments, the model was trained on the HHB_v05, HHB_v06, and HHB_v07 datasets and tested

on the STHBC_[A–H], ViHBC, XeHBC, and IDC datasets following the original paper’s inference procedure. We followed the training data selection strategy as described in the original study, which uses these specific reference datasets, rather than the full range HHB_[v03–v10]. For the CRC datasets, the training and inference datasets were the same as those used for MEATRD. All other settings and hyperparameters followed the original STANDS implementation as described in the original paper.

SpaCell-Plus is an extended version of SpaCell, designed to support cross-platform CTR detection by incorporating transfer learning. Specifically, it extracts features from 299×299 histology image patches using ResNet50 and processes them in parallel with the gene count matrix of each ST spot through two completely independent autoencoders. The resulting latent vectors of equal dimension are concatenated and fed into the same cancer likelihood discriminator as

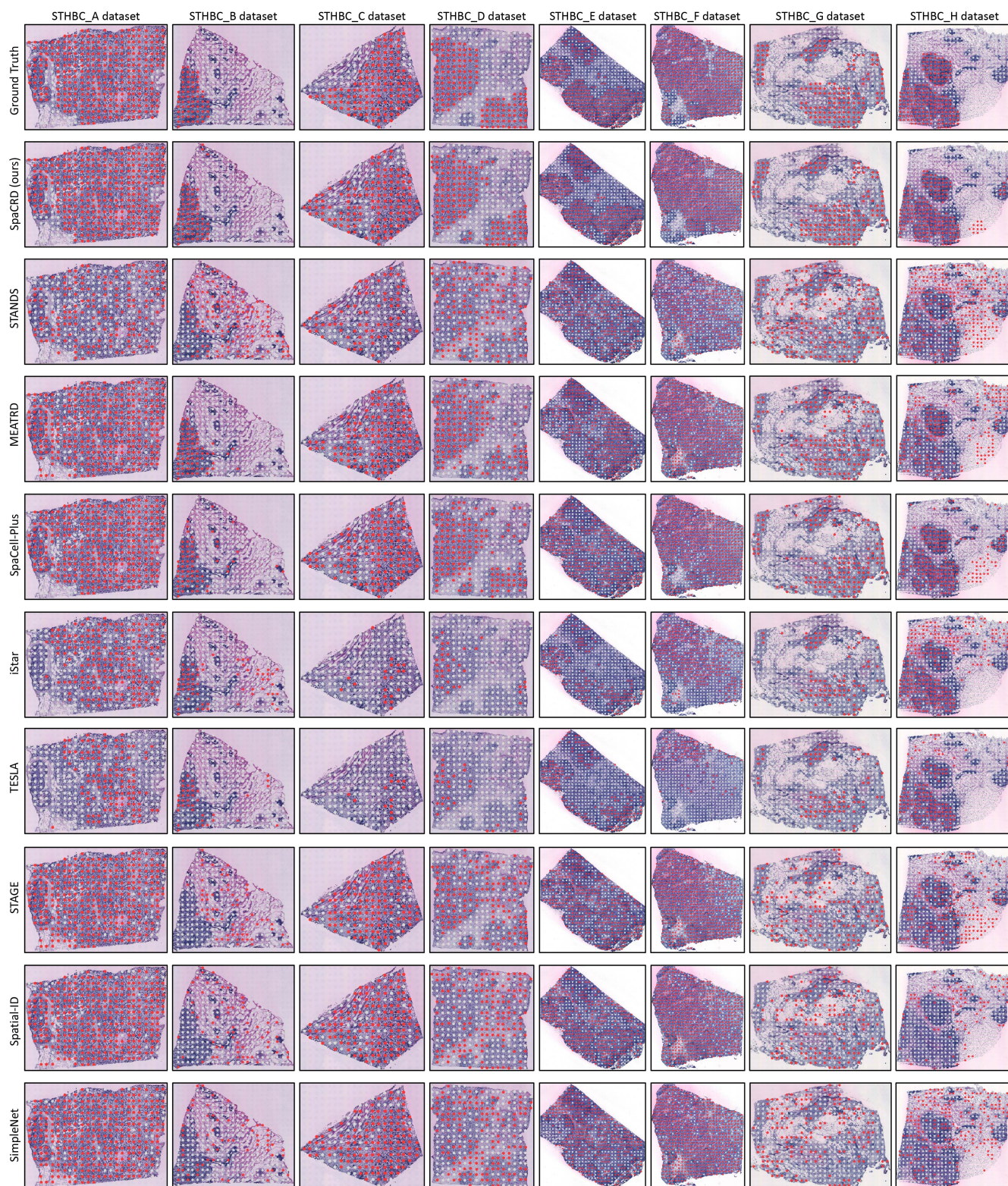


Figure S1: ATR detection results of SpaCRD and other baselines on the eight STHBC datasets. Gray and red dots represent normal and cancerous spots, respectively.

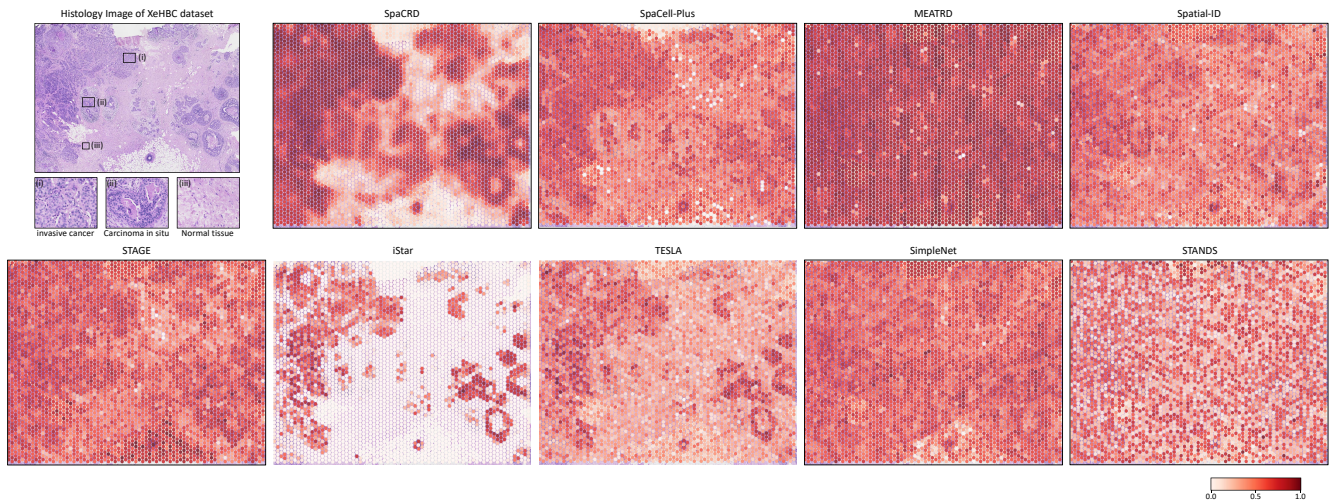


Figure S2: Visualization of cancer likelihood scores predicted by SpaCRD and other baselines on the XehBC dataset.

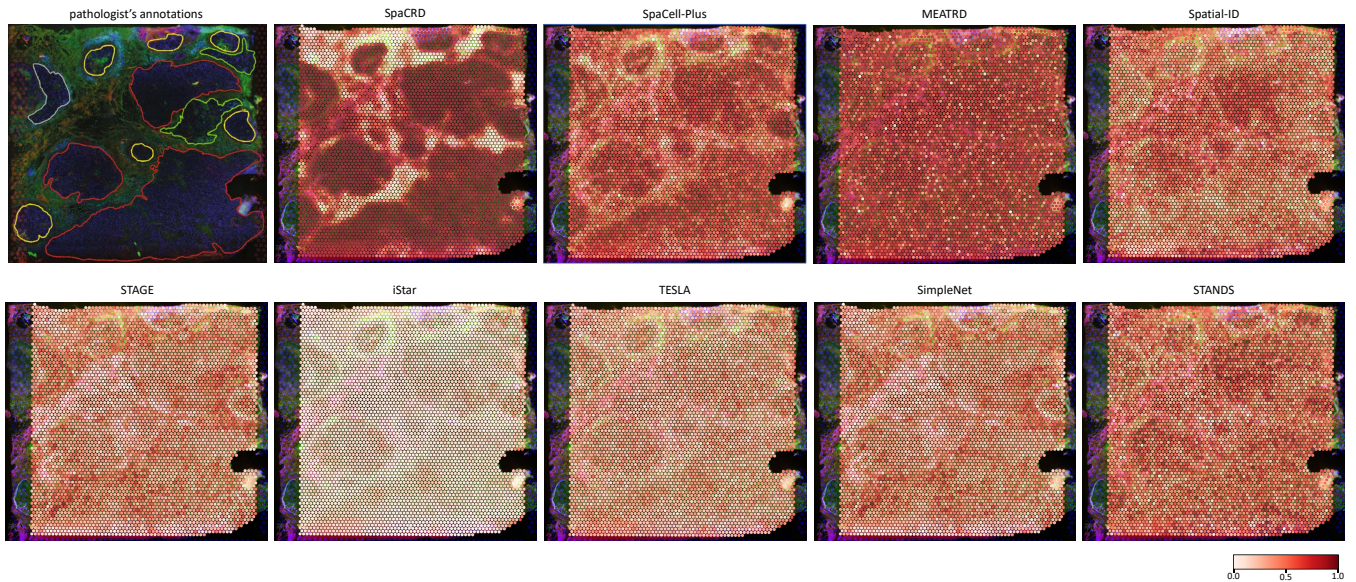


Figure S3: Visualization of cancer likelihood scores predicted by SpaCRD and other baselines on the IDC dataset.

used in our method for prediction. While retaining the original architecture of SpaCell, SpaCell-Plus replaces the unsupervised training paradigm with a transfer learning strategy. To ensure a fair comparison, SpaCell-Plus was trained and tested on the same datasets as SpaCRD.

iStar primarily relies on expert-defined prior knowledge to perform CTR detection. It identifies cancer-epithelial cells by comparing predefined marker gene lists with the gene expression profiles in the ST data. The model architecture of iStar primarily consists of a pre-trained HIPT module for extracting hierarchical histology features, followed by a feedforward neural network for predicting super-resolution gene expression. To enable benchmark-compatible CTR detection, we aggregate the cancer-epithelial likelihood scores of all superpixels covered by each Visium-scale spot, based

on the spot size and spatial distribution pattern defined by the Visium platform. Since iStar is entirely based on prior knowledge, it does not require training data and can be directly applied to the test datasets for inference.

TESLA relies primarily on expert-defined prior knowledge for tumor region detection. It infers cancer regions by comparing predefined tumor marker gene lists with a super-resolution gene expression map imputed from low-resolution ST data and H&E-stained histology images. The model architecture comprises two main components: (i) a superpixel-level gene expression imputation module that integrates spatial proximity and histological similarity, and (ii) a lightweight CNN that segments tumor regions based on a meta-gene image concatenated with the grayscale histology. To ensure compatibility with benchmark evaluations, cancer

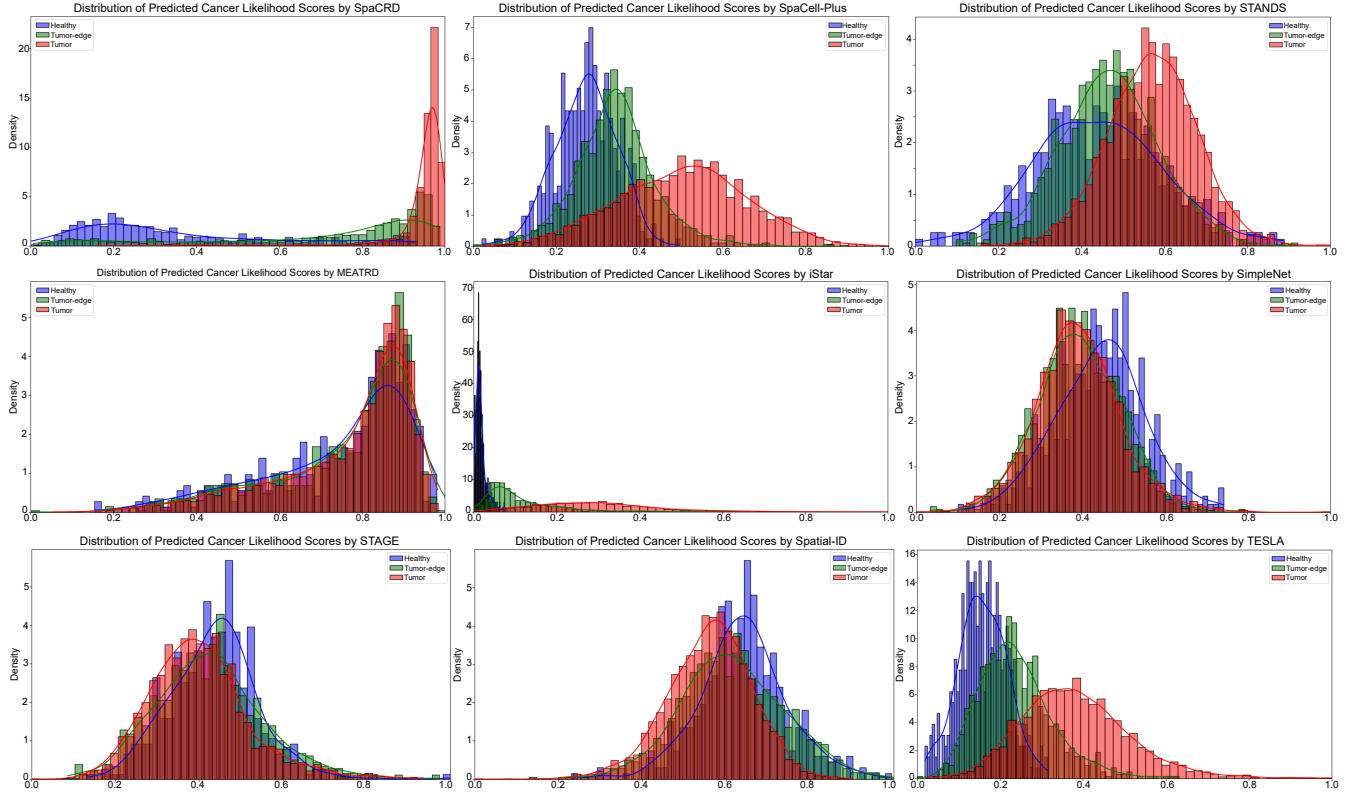


Figure S4: Histograms of predicted cancer likelihood scores by SpaCRD and other baselines on the ViHBC dataset, grouped by three region types: healthy, tumor, and tumor boundary, based on ground truth.

likelihood scores from all superpixels within each Visium-scale spot are aggregated according to the spot geometry and spatial layout defined by the Visium platform. As TESLA is fully prior-driven, it does not require any training data and can be directly applied to test datasets for inference.

STAGE was originally designed to impute gene expression at unmeasured locations in spatial transcriptomics by integrating spatial coordinates and gene expression through a spatially supervised autoencoder. Specifically, the model encodes gene expression profiles into latent representations, which are trained to reconstruct the original inputs under the supervision of spot coordinates. In our adaptation for CTR detection, we replace the spatial supervision with binary labels indicating cancerous or non-cancerous spots, thereby modeling the latent representation as a cancer/healthy embedding. We further adopt a transfer learning strategy, enabling the model to generalize across datasets.

Spatial-ID is a spatial clustering method designed to distinguish between cancerous and healthy spots. It first trains a deep neural network (DNN) using annotated scRNA-seq data to generate cell type probability distributions as pseudo-labels. Then, a spatial adjacency graph is constructed, and a variational graph autoencoder (VGAE) is employed to integrate gene expression with spatial coordinates. A self-supervised learning scheme is used to optimize a cell-type classifier, which ultimately identifies ambiguous spots with low maximum assignment probabilities. Since Spatial-ID re-

lies on scRNA-seq data for pretraining, we adopt the publicly available pretrained model and skip the training-from-scratch stage in our implementation.

SimpleNet is a lightweight anomaly (i.e., cancer) detection framework consisting of a pretrained feature extractor, a single fully connected feature adapter, a Gaussian noise-based anomaly generator, and a two-layer MLP discriminator. It introduces random noise into embedded visual features and trains a hyperplane-based discriminative factor to separate pseudo-anomalies from normal samples. For fair comparison, SimpleNet is evaluated using the same dataset partitioning as MEATRD.

S7 Evaluation Metrics

To comprehensively evaluate the performance of SpaCRD in CTR detection, we employ four standard classification metrics: Area Under the Receiver Operating Characteristic curve (AUC), Average Precision (AP), F1-score, and Kolmogorov-Smirnov (KS) distance.

Area Under the ROC Curve (AUC) measures the area under the receiver operating characteristic curve, which plots the true positive rate against the false positive rate across all classification thresholds. It is mathematically defined as:

$$\text{AUC} = \int_0^1 \text{TPR}(t) d\text{FPR}(t), \quad (\text{S12})$$

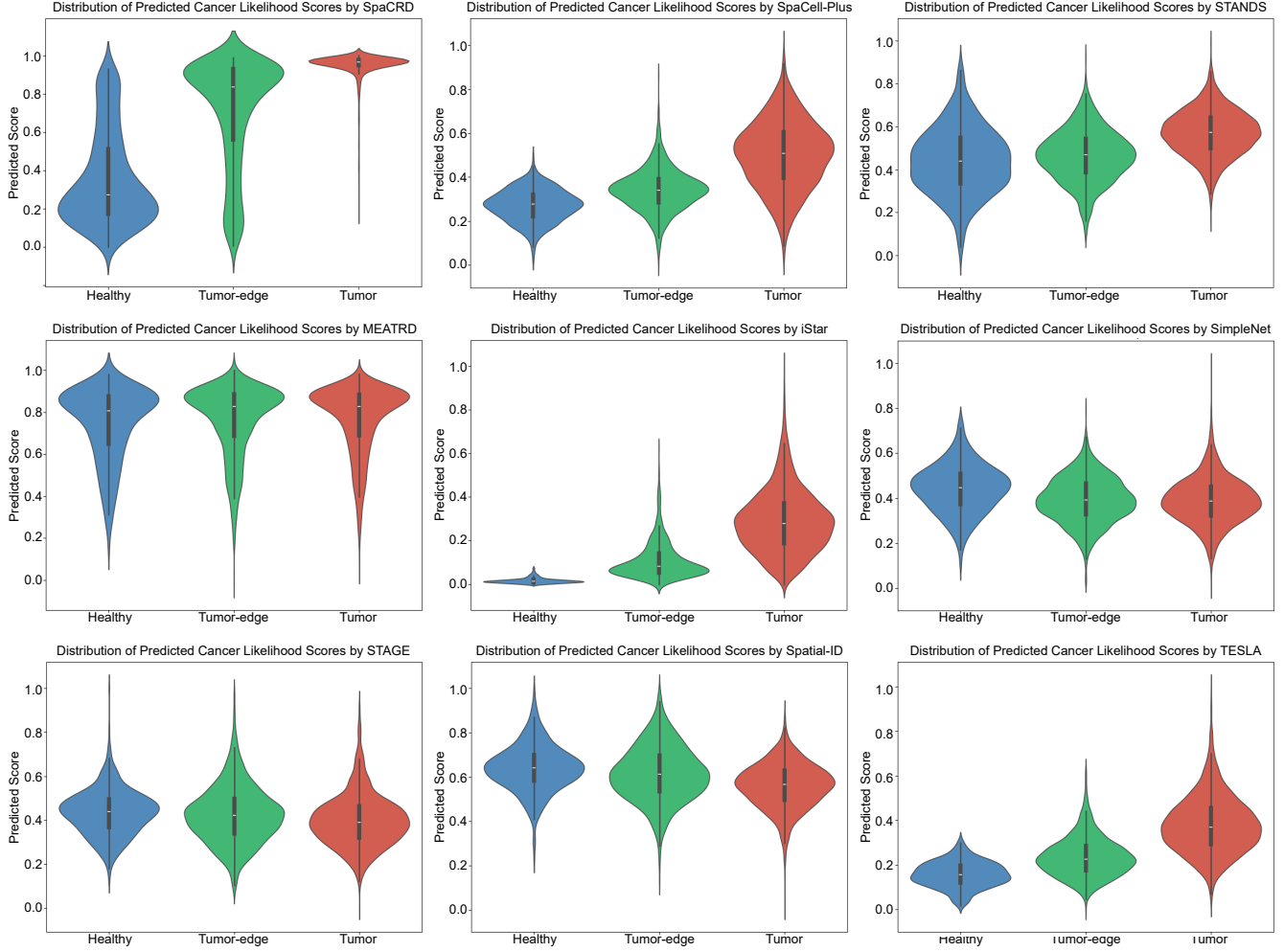


Figure S5: Violin plots of predicted cancer likelihood scores by SpaCRD and other baselines on the ViHBC dataset, grouped by three region types: healthy, tumor, and tumor boundary, based on ground truth.

where $\text{TPR}(t) = \frac{\text{TP}(t)}{\text{TP}(t) + \text{FN}(t)}$ and $\text{FPR}(t) = \frac{\text{FP}(t)}{\text{FP}(t) + \text{TN}(t)}$ represent the true positive rate and false positive rate at threshold t , respectively. AUC ranges from 0 to 1, with higher values indicating superior discriminative capability across all operating points.

Average Precision (AP) summarizes the precision-recall curve by computing the area under it, providing a single scalar that captures performance across all recall levels:

$$\text{AP} = \int_0^1 P(r) dr = \sum_{k=1}^n P_k \Delta R_k, \quad (\text{S13})$$

where P_k and $\Delta R_k = R_k - R_{k-1}$ denote the precision and recall increment at the k -th threshold, respectively. AP is particularly valuable for imbalanced datasets where the minority class (positive samples) is of primary interest.

F1-score represents the harmonic mean of precision and recall, providing a balanced measure that accounts for both

false positives and false negatives:

$$\text{F1} = \frac{2 \cdot \text{Precision} \cdot \text{Recall}}{\text{Precision} + \text{Recall}} = \frac{2\text{TP}}{2\text{TP} + \text{FP} + \text{FN}}, \quad (\text{S14})$$

where $\text{Precision} = \frac{\text{TP}}{\text{TP} + \text{FP}}$ and $\text{Recall} = \frac{\text{TP}}{\text{TP} + \text{FN}}$. To ensure a fair comparison, the F1-score was computed using a threshold that matches the actual proportion of true positives in the ground truth.

Kolmogorov-Smirnov (KS) distance quantifies the difference between two distributions by finding the largest gap between their cumulative distribution functions. A KS distance near 1 signifies strong separation between the distributions. It is mathematically defined as:

$$D_{\text{KS}} = \sup_x |F(x) - G(x)| \quad (\text{S15})$$

where \sup_x denotes the supremum over all values of x .

Method	Params	Training Time (s)	Inference Time (s)	Memory Usage (MB)
SpaCRD (Ours)	8.70M	33.86	1.15	535.68
MEATRD	48.61M	1378.70	13.35	8401.39
STANDS	68.19M	986.77	12.89	18426.91
SpaCell-Plus	1.72M	44.25	0.06	94.14
iStar	2.41M	222.03	11.98	325.15
TESLA	5.68M	5790.68	18.71	7619.64
STAGE	5.21M	770.06	0.12	60.36
SimpleNet	75.63M	1.66	10.27	1.28
Spatial-ID	4.12M	967.18	1.16	0.37

Table S2: Comparison of computational cost on the ViHBC dataset among all methods.

S8 Further Results

S8.1 Visualization of CTR Detection Results

We further demonstrate the clear superiority of SpaCRD over all baseline methods by visualizing the CTR detection results on the eight STHBC_[A-H] datasets. As shown in Figure S1, SpaCRD achieves the highest consistency with ground-truth CTR annotations in most datasets. Its superiority is especially pronounced in challenging cases involving multiple spatially disconnected CTR, such as STHBC_D, STHBC_E, and STHBC_G.

Subsequently, we visualized the cancer likelihood scores predicted by SpaCRD and all baseline methods on the XeHBC and IDC datasets to further assess their performance on cross-platform&batch CTR detection. As shown in Figure S2 and S3, SpaCRD not only effectively separates normal and cancerous tissue regions, but also captures differences in cancer severity based on the magnitude of the predicted likelihood scores (e.g., distinguishing between invasive carcinoma and carcinoma in situ). In contrast, although other methods can to some extent distinguish cancerous regions from normal tissue, their predicted boundaries are often overly blurred, and the likelihood scores show insufficient separation among invasive carcinoma, carcinoma in situ, and normal regions. Such limitations are inadequate for CTR detection tasks that require high accuracy.

S8.2 Distribution Analysis of Cancer Likelihood Scores Across Tissue Regions

To further evaluate the performance of SpaCRD, we performed a distribution analysis of cancer likelihood scores on the ViHBC dataset, which contains manual annotations dividing the tissue into three distinct regions: healthy, tumor, and tumor-edge. We analyzed the cancer likelihood scores of spots within each annotated region to assess the ability of different methods to distinguish these biologically meaningful areas. As shown in Figure S4, SpaCRD effectively distinguishes between healthy and tumor regions, with the predicted cancer likelihood scores exhibiting well-separated distributions (Mean: healthy=0.35, tumor-edge=0.70, tumor=0.94; Mode: healthy=0.19, tumor-edge=0.91, tumor=0.97). SpaCRD predicts tumor-edge regions with likelihood scores closer to tumor regions, reflecting that these edge regions are transitional zones that may warrant special attention due to potential pathological changes. In contrast, other methods such as SpaCell-Plus (Mean: healthy=0.27, tumor-edge=0.34, tumor=0.50;

Mode: healthy=0.28, tumor-edge=0.34, tumor=0.53) and iStar (Mean: healthy=0.02, tumor-edge=0.11, tumor=0.28; Mode: healthy=0.01, tumor-edge=0.06, tumor=0.28) show smaller separations in predicted scores across the three regions, suggesting weaker contrast between healthy, tumor-edge, and tumor spots. Furthermore, as shown in Figure S4, the predicted scores for spots across the three regions are highly overlapping in other baseline methods, making it difficult to clearly distinguish between healthy, tumor-edge, and tumor regions. To further highlight the advantages of SpaCRD, we visualized the distributions of the three regions using violin plots. As shown in Figure S5, SpaCRD (top-left) demonstrates a clear separation among the predicted cancer likelihood scores for healthy, tumor-edge, and tumor regions. The healthy spots mostly have low scores, tumor-edge spots show intermediate scores closer to tumor regions, and tumor spots have high scores approaching 1.0. This distribution aligns well with the biological progression from healthy to tumor states, especially highlighting the transitional nature of tumor-edge regions.

Finally, we evaluated the distributional divergence between predicted cancer likelihood scores in healthy and tumor regions across the eight STHBC datasets using the KS distance. As shown in Figure 4 of the main text, SpaCRD exhibited the strongest separation between healthy and tumor regions across most STHBC datasets (Median: SpaCRD=0.754, SpaCell-Plus=0.494, MEATRD=0.348, TESLA=0.366, STAGE=0.273, SimpleNet=0.264, iStar=0.354, Spatial-ID=0.186, STANDS=0.127). Overall, these results demonstrate the superior capability of SpaCRD to accurately reflect the underlying biological differences between healthy and tumor spots, which is critical for precise CTR detection.

S8.3 Sensitivity Analysis

We conducted a sensitivity analysis on three key components: the directional weighting coefficient α for contrastive loss in modality-alignment representation learning, the category-regularized KL divergence loss weight β , and the multimodal fused loss weight γ in the cancer likelihood discriminator. Table 5 of the main text shows the average model performance over five independent runs across eleven breast cancer datasets. We observed that setting $\alpha = 0.5$ yields the best performance. This result highlights the benefit of jointly modeling bidirectional modality alignment. However, the model remains relatively robust when using $\alpha = 0$ or $\alpha = 1$, with only minor performance differences. For the category-regularized KL divergence loss, we observed that setting $\beta = 0.5$ achieves strong performance. Increasing β to 1.0 only slightly decreases the performance, whereas reducing it to 0.1 leads to a notable drop. This indicates that incorporating a moderate level of class-aware regularization is essential for downstream cancer region identification. Setting γ to 0 results in a substantial performance degradation, as omitting the fused loss enables the cancer likelihood discriminator to adversely affect the latent space, causing overfitting. Finally, we found that selecting 6 neighboring spots in the BCA module achieves optimal performance, consistent with the hexagonal arrangement of ST

Training data	ViHBC			XeHBC			IDC		
	AUC	AP	F1	AUC	AP	F1	AUC	AP	F1
C (176 spots)	0.861±0.029	0.882±0.035	0.817±0.018	0.875±0.022	0.749±0.047	0.731±0.038	0.779±0.034	0.783±0.36	0.757±0.41
D (306 spots)	0.888±0.016	0.913±0.016	0.863±0.010	0.911±0.016	0.820±0.037	0.759±0.025	0.867±0.021	0.886±0.26	0.833±0.36
Full (3,481 spots)	0.900±0.029	0.930±0.037	0.867±0.014	0.931±0.008	0.859±0.021	0.795±0.013	0.891±0.006	0.914±0.006	0.854±0.008

Table S3: Small-sample training analysis results on the ViHBC, XeHBC, and IDC datasets.

data. Although performance slightly decreases when selecting 4 or 8 neighbors, it remains stable, demonstrating the robustness of our model to the choice of neighborhood size.

S8.4 Empirical Efficiency Analysis

We compared the empirical efficiency analysis of SpaCRD with all baseline methods. As shown in Table S2, all models were trained on eight STHBC datasets and tested on ViHBC dataset. SpaCRD uses a moderate number of parameters (8.70M) and achieves much faster training (33.86 s) and inference times (1.15 s) than larger models like MEATRD and STANDS, while consuming significantly less memory (535.68 MB). Compared to lightweight models such as SpaCell-Plus and STAGE, SpaCRD maintains a good balance between runtime efficiency and resource usage. These results indicate that SpaCRD maintains an acceptable computational cost.

S8.5 Small-Sample Training Analysis

We conducted a small-sample training analysis on the eleven breast cancer datasets. In our main experiments, the model was trained on all eight STHBC datasets (3,481 spots) and evaluated on three test datasets (ViHBC, XeHBC, and IDC), each containing between 3,798 and 4,727 spots. To further investigate the effect of training data scale, we conducted additional experiments with significantly reduced training samples. Specifically, we trained our model on much smaller subsets—176 spots from the STHBC_C dataset and 306 spots from the STHBC_D dataset. As shown in Table S3, although performance declined slightly under these conditions, the drop was not substantial, demonstrating that our model is robust and does not heavily rely on large-scale training data.